Multi-Phase Flow Modeling Capability with Chemical Kinetics

T. Dunn, J. Ortega, D. Flowers, T. Piggott, K. Wittaker, R. Couch

The purpose of this project was to enhance LLNL's fluid dynamics capability in the area of multi-phase and chemically reacting flow. This was accomplished by building upon the current tools available in the ALE3D multi-physics hydrocode. The project focused on discrete particulate transport, free-surface flows, and chemical kinetics. Verification and validation were emphasized to provide confidence in the accuracy of the methods.

The particle-tracking module was developed to simulate problems involving particulate transport within a carrier fluid. Dilute particle flow is assumed where local aerodynamic forces control the particle's motion and particle-particle interactions are neglected. Momentum is transferred from the particle to the fluid through the fluid's continuum equations. Each particle is individually tracked in a Lagrangian reference frame using an equation of motion derived from Newton's second law. The equation accounts for the steady-state aerodynamic and gravity/buoyancy forces acting on the particle, as well as pressure and shear gradients within the flow-field. A random-walk model was developed to predict turbulent dispersion of the particles (Fig. 1). An inelastic hard-sphere bounce model is used for particle-wall interaction. Additional physics may be easily added to the model by adding additional terms to the particle's equation of motion.

Droplet dynamics has been the main thrust of the free-surface modeling effort. The deformation and breakup of droplets involve complex coupling between aerodynamic forces and the droplet response. The Arbitrary-Lagrangian-Eulerian (ALE) formulation in ALE3D is ideally suited to model the droplet motion. A surface-tension model was added to ALE3D to simulate the intermolecular forces within the droplet. In addition, a mesh-relaxation scheme was added such that the computational grid surrounding the droplet is mapped to the droplet motion and a constant level of grid refinement near the surface is obtained throughout the simulation. Another method consisted of an interface-tracking algorithm for fluid/droplet interfaces that do not conform to mesh boundaries.

Another aspect of this project was to explore ALE3D's capability to handle coupled fluid mechanics and chemically reacting flow by modeling hydrogen-oxygen detonation in a shocktube. This involves complex interaction between shock waves, contact discontinuities and expansion waves, and the chemistry of combustion. First, a 1-D model was used to quantify the capabilities and limitations of ALE3D. The calculations showed a large temperature overshoot at the contact discontinuity, as well as temperature oscillations after the shock (Fig. 2). Additional 2-D simulations including the reaction of an H_2-O_2 mixture were also performed.

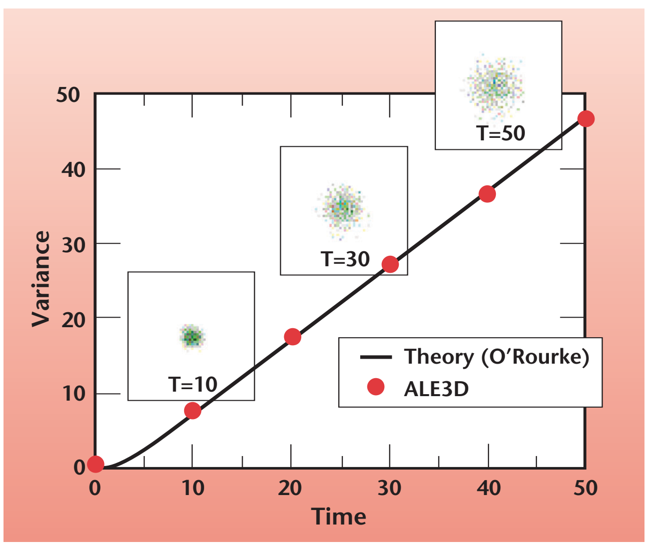

Figure 1. *Theoretical and calculated variances in the distributions of drop position. The calculations used 1000 particles released from a point source.*

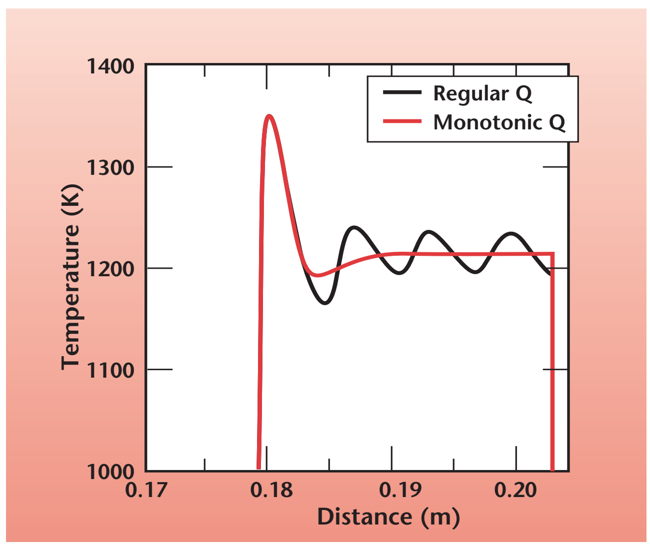

Figure 2. *Calculations of a hydrogen-oxygen detonation in a shocktube, showing the effect of artificial viscosity (Q) on the temperature prediction.*

Model-Based Manufacturing

R. N. Frank, M. Prokosch

The goal of the FY02 Model-Based Manufacturing (MBM) Project was to improve skills and procedures for "paperless" manufacturing within the Manufacturing and Materials Engineering Division at LLNL. The primary focus was to establish Pro/Engineer as a business tool within the Main Bay facility.

We purchased a modern workstation for the Main Bay Planner and another for the Programmer. We acquired Pro/E licenses for those workstations, and an ICAM post-processor license. The post-processor is required to translate generic numerical control (NC) code into machine specific code. The software was installed and configured.

We obtained Pro/E training for the Main Bay personnel as well as one Inspector (funded independently). Once the basic Pro/E skills were established, we contracted with a recognized expert in NC programming from Sandia National Laboratory to give a one week, hands-on class at LLNL. All the participants felt this was an outstanding session and we hope to repeat it at a more advanced level this year.

The bulk of this project did not occur in a laboratory environment, but rather on the program-driven shop floor. Scheduling difficulties and programmatic work delayed the completion of the Pro/E training until early May. Post-processor development is done in-house and a heavy workload in the NC Shop also impeded development until late in the fiscal year. In spite of these factors, we were able to develop a functional expertise with the technology by the end of the year.

Early in the project we received MBM projects from Laboratory programs. The increase in our skills, knowledge, and ability were highly evident. We were unable to exactly account for the time required to manufacture a part at each phase, but the part took well less than half as long to complete the second time we did it. Past experience dictates that this efficiency will continue to increase as MBM becomes a routine business method.

The MBM project also had a larger scope. Laboratory personnel concerned with Computer Integrated Manufacturing met to discuss MBM issues during the life of the project. Since MBM uses relatively raw data from designers, a common interface needs to be forged between design and manufacturing. In traditional methods, the formal drawing is that interface. In MBM, the model fills that role and must satisfy both groups.

Through these discussions and practical experience we began a MBM specification for LLNL. This document will serve as a guideline for designers and manufacturers to incorporate design for manufacturability techniques into a model. This will reduce the cost of detail drawing, yet provide sufficient information for accurate and efficient fabrication. We expect to have a draft ready for review and submission in the near future.

This project gave us the opportunity to purchase the tools and training we needed to incorporate an important technology into our main manufacturing facility. We enhanced the MBM capabilities in the NC Shop and are looking forward to developing Model-Based Inspection.

Furthermore, the project brought several very talented people from different organizations together. This combination of technology, training, and collaboration laid a solid foundation for a technology that promises to deliver critical products for our customers faster, better, and cheaper than before.

Computational Mechanical Engineering Tools

C. Hoover, R. Ferencz

Current code-enhancement activities include adding and improving models for elements and materials to more adequately describe the behavior of foam, rubber, viscoelastic explosives, and layered composite materials. Contact algorithm development for improving the treatment of material interfaces is an ongoing activity.

Sophisticated computational mechanics tools are an essential part of a mechanical engineer's analysis and problem solving strategy. LLNL's Methods Development Group and Thermal Fluids Group develop nonlinear finite-element codes (NIKE3D, DYNA3D, TOPAZ3D, ParaDyn, Diablo) for solid, structural, and thermal/fluid analysis. In addition, the two groups support the analysts' activities with individual consulting, up-to-date online documentation, and training classes.

Progress in FY02 is described in part in articles by Lin, Puso, Speck, and Shapiro, elsewhere in this Volume.

New capabilities in the visualization software are based on a flexible binary database format generated by the Mili I/O library and supported with the GRIZ4 visualization tool. The latest database development and enhancements provide the ability to visualize time-history results and coupled results from analysis programs, and conveniently add new results to the databases.

A new anisotropic fracture mechanics material model used for rock mechanics and other fracture mechanics applications benefited from the design flexibility of the database.

A frequent requirement of high-fidelity simulation is combining the effects of relatively slow processes, *e.g.*, assembly loads from bolts, or gravity load, with the effects from rapid events that characterize the service life or possible accident scenarios such as rapid pressurization or earthquake loading.

The figure shows a representative analysis of a containment vessel that couples pre-load results calculated in NIKE3D with a time-dependent analysis using DYNA3D. The purpose of these calculations was to measure the stress on the bolts for different types of loads and for an envelope of expected load levels for each type of load. To include the detail needed in the analysis, the size of this mesh was 300,000 elements. The next calculation of a containment vessel is expected to be twice as large, suggesting the need for a coupled parallel analysis using the NIKE3D program with a parallel linear solver coupled to ParaDyn.

Early in FY02 we sponsored a four-day class to meet the training needs of newly-hired analysts and to keep our experienced analysts up-to-date. The class included a one-and-a-half-hour lecture for each software product, an introductory lecture on the theoretical background for finite-element analysis, and an overview of the Diablo code development.

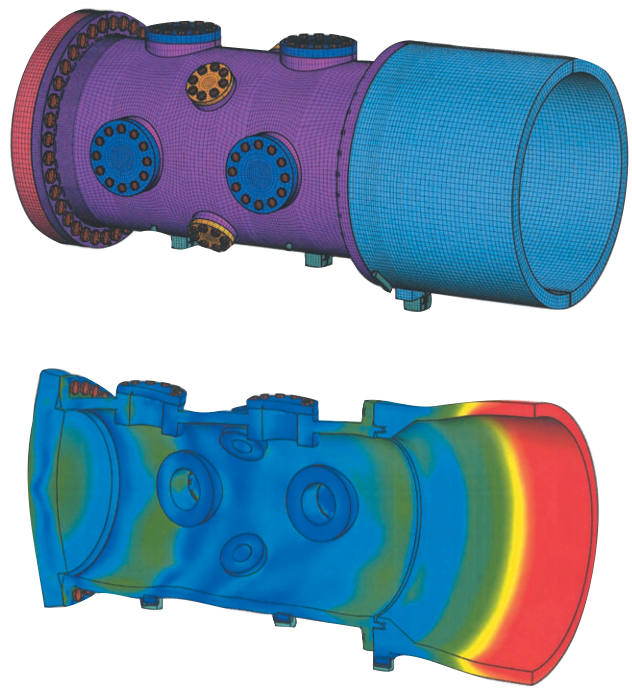

Representative analysis of a containment vessel. The containment vessel for the Piano sub-critical test apparatus required detailed examination of the effects of both bolt pre-loads and subsequent rapid internal pressurization. Both the detail of the mesh and the stresses created by internal pressurization are highlighted. Deformations are magnified in the lower image.

Capability Enhancements in NIKE3D

M. A. Puso

In FY02, we added features and efficiency improvement to NIKE3D, in support of multiple applications. This report highlights new plasticity models and algorithmic enhancements that led to large performance increases.

Two new hyper-elasto-plastic material models were implemented. These models are derived from strain energy functions and thus guarantee proper thermodynamic behavior in large strains. This improves upon the older, common hypo-elasto-plastic models that can display anomalous behavior, especially in cyclic loading and unloading. Exact linearizations were derived and implemented and provide more rapid convergence for nonlinear problems.

The figure illustrates this improved performance for a model problem of a copper bar undergoing large deformation due to impact.

An important issue in implicit finite-element technology for nonlinear problems is the inclusion of the so-called geometric stiffness arising from the internal state of stress in a body. That a violin string takes on a higher pitch as it is tightened is a common manifestation of this effect, but it can be important in many situations. Buckling is another phenomenon related to this effect.

Unfortunately, always including the geometric stiffness can slow convergence or even algorithmically destabilize some nonlinear analyses. In support of modeling an x-ray columnator, a thin-walled structure, new logic was implemented for activation of the geometric stiffness in NIKE3D. This logic delays inclusion of the geometric stiffness until the energy norm reaches a prescribed threshold. For the columnator analysis, this reduced the number of time steps from 200 to 8, reducing the execution time by a factor of 15.

Two new enhancements were motivated by on-going efforts (reported elsewhere in this volume) to model a concrete, segmented arch dam. A special contact algorithm to mimic the effect of an interlocking "key joint" was prototyped to establish feasibility, then fully implemented with project funds. This capability will permit the modeling of key ratchet without using many small elements to capture the detail of the joint geometry. The dam/reservoir/canyon model involved contact facets and initialization of the model was slow. To avoid the N^2 search previously required to identify elements, and thus a material stiffness, for each contact facet, an inverse node-to-element map is now computed. This was found to speed up the contact initialization by roughly a factor of 100.

Clearly, all large models will benefit from this improvement.

(a)

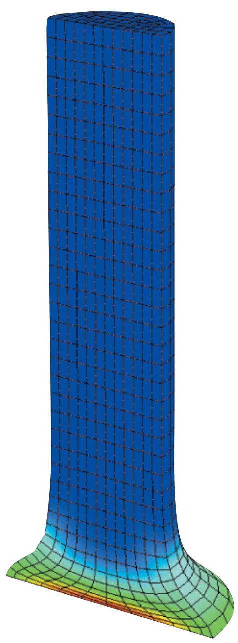

(b)

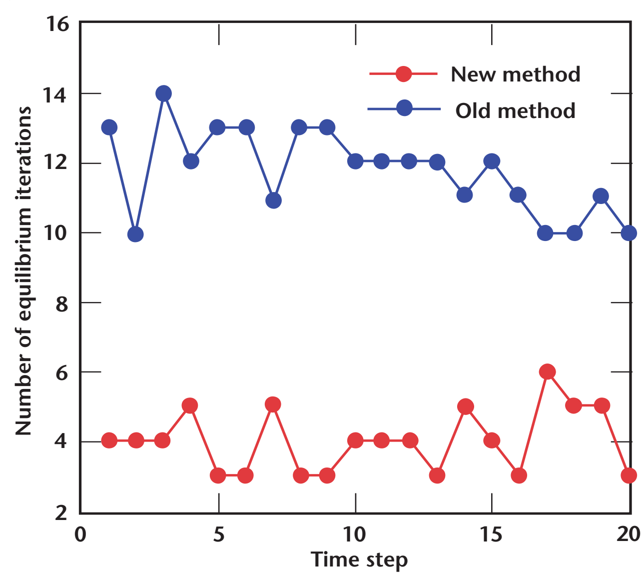

(a) NIKE3D Taylor bar simulation. (b) Number of equilibrium iterations per time step with old and new plasticity algorithms for the simulation. The new algorithm requires far fewer iterations, and is therefore much more efficient and robust.

Heat Transfer and Fluid Code Enhancement

A. Shapiro

We have extended the capabilities of Topaz2d, TEXSTAN, and Topaz3d.

Topaz2d

A major effort, started in FY01, was the addition of a new slide-line algorithm in Topaz2d. This was driven by the needs of a defense program activity. The existing algorithm was intended for master and slave surfaces that start and end at the same spatial location. This condition is not overly restrictive for heat transfer problems since no motion is taking place due to applied forces.

However, for the W80, a mechanical mesh was created consisting of 83 slide surfaces, for which many slave-master pairs did not meet the condition of identical starting and ending points. This high-fidelity mechanical model was also to be used as a thermal model. A new slide-surface algorithm was implemented in which the slave and master surfaces could start and end at arbitrary locations.

The method is a surface-to-surface algorithm, as opposed to the simpler node-to-surface algorithm currently in Topaz2d. The algorithm maps (*i.e.*, finds the shadow of) the smaller surface area of the slave-to-master pair onto the larger surface. This shadow area is called the contact area, A_c. The heat transfer between the surfaces is then calculated by $\dot{q} = hA_c(T_m – T_s)$ where T_m and T_s are the temperature of the master and slave surfaces, respectively. The heat transfer coefficient, h, can be defined as a convection conductance, a radiation conductance, or a combination of both.

TEXSTAN

TEXSTAN is a code that calculates the momentum and energy boundary layer for slab and axi-symmetric geometries. The code was obtained several years ago from the University of Texas. The code is used by the Mercury Laser Project to determine convection heat transfer coefficients and predict flow separation in the gas-cooled amplifier units. Several bugs were fixed in the code during porting of the code to SGI UNIX. Verification and validation were performed on the code by comparing calculated results for the various turbulence models to analytical solutions.

Topaz3d

Input file formats for integer variables have been set to I5 (*i.e.*, five integer digits are to be read). This places an upper bound on the finite-element model size of no more than 99,999 elements and 99,999 nodes. Recent models, such as the amplifier end-effects thermal-recovery unit (shown in the figure) required more than 120,000 elements. The entire input structure of Topaz3d was modified such that integers would be read in I8 (*i.e.*, eight integer digits) format. This will allow up to 99,999,999 elements and nodes in a model.

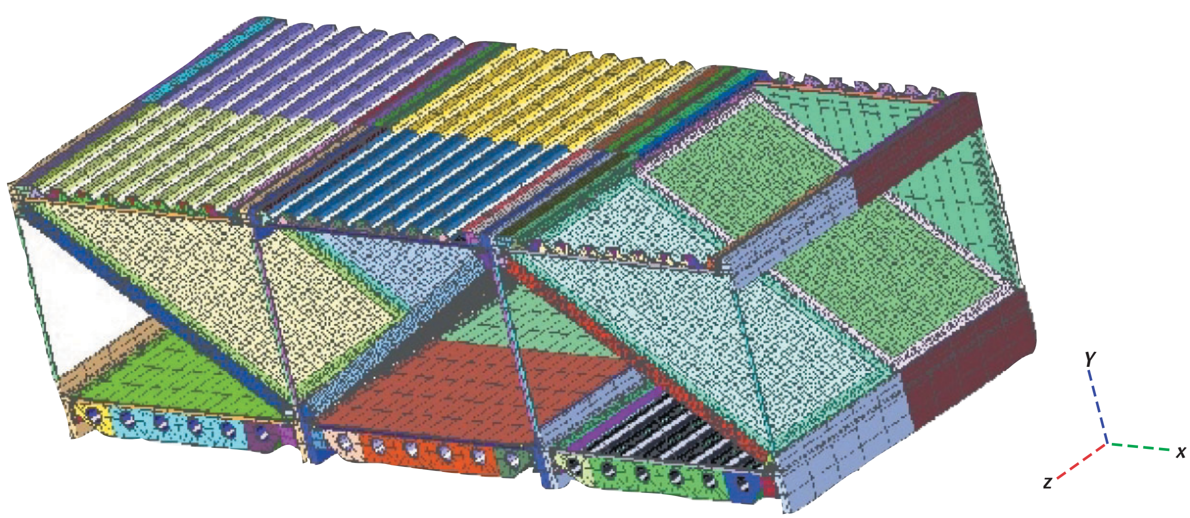

Model of laser amplifier end-effects recovery unit.

Post-Processing and Data Management Activities

D. Speck

An important improvement in FY02 was the creation of an initial Mili version of the TAURUS time-history database, which is paving the way to have a single tool (GRIZ) post-process both plot and time-history databases.

This year's trend to 64-bit computing impacted graphics and data management software in multiple ways. Both the GRIZ finite-element post-processor and the Mili I/O library were updated to have 64-bit "clean" source code. GRIZ was further enhanced with an initial capability to accommodate double-precision simulation data from Mili databases, with the addition of code to convert such data to single-precision as it is read in. This will enable GRIZ to visualize the analysis code link files used to communicate simulation data between analysis applications.

One desirable capability that has been identified since the initial implementation of Mili and version 4 of GRIZ is the ability to define and write data associated with surfaces. The surfaces of interest might be boundary condition surfaces, contact surfaces, or rigid walls. These are data managed in the analysis, but heretofore they have lacked a natural form of expression in Mili or logic for post-processing in GRIZ.

One of the major accomplishments in FY02 was the implementation of a surface "superclass" in Mili, plus initial supporting logic in GRIZ, to load and manage surfaces and the simulation data associated with them. This new code is being tested and integrated with the production source.

Experience to date with Mili version 1.0 has demonstrated areas where additional new capability is required, as well as areas where the existing design can be improved in terms of its generality, correctness, or efficiency. These new and improved capabilities have been collected and documented to define the requirements for Mili version 2.0.

In FY02, we developed a Mili 2.0 requirements and design document. A version 2.0 development branch was created in the Mili source code repository and implementation of Mili 2.0 was initiated.

An important aspect of the Mili 2.0 effort is a move to improve the overall quality of the code and limit debugging time in later development stages by instituting proven software quality assurance practices. One practice, already described, is the explicit documentation and review of both requirements and design for the new Mili version.

Another new practice is the integration of application code and unit-testing modules so that new code can be tested throughout its lifetime. A third practice planned is that of code reviews in which new code is circulated among cognizant developers for critical feedback.

One software engineering practice that supports improved quality is formal change control. We have used SCRTrack for several years to manage software change requests (SCRs). Most of the use of SCRTrack has been devoted to GRIZ and Mili activities. In FY02, 41 SCRs were resolved: 29 for GRIZ and 12 for Mili. Of these, 11 originated with GRIZ/Mili developers, 12 originated with other code developers, and 18 originated with engineering analysts. There were 31 new SCR's defined in FY02 that went unresolved, but of these, only eight were bug reports (the rest were enhancement requests), and none of the eight was critical.

In FY02, two trends can be identified among the forces driving post-processing and data management code development activities at LLNL. One is a more thorough exercising of GRIZ (and implicitly, Mili) by the new engineering analysts. These users have no preconceptions about how the codes should behave, nor have they established patterns of use that might limit their exploration of new features in the code. These characteristics lead to valuable new insights and perspectives on code behavior, as well as the discovery of both new and long-hidden bugs.

Another trend has been analysis using Mili, which affects Mili directly and GRIZ indirectly. As the new implicit analysis code, Diablo, matures and an expanding set of material-model-specific simulation data from ParaDyn/DYNA3D are expressed in the Mili database, features planned for years ago are finally being exercised. At the same time, equally important (and unanticipated) new requirements are being generated that will increase Mili's utility and value in the years to come.

Gas-Induced Pressure Loads in DYNA3D

J. Lin

We have added new features to DYNA3D for structural analysis of gas-induced pressure loads.

In structural analysis of mechanical systems, one often encounters the modeling of gas-filled chamber-like structures. The pressure load imposed on the structure by the enclosed gas will change because of the addition of more gas into the chamber or the change of the chamber volume. The obvious examples for the former are the gun barrel and the vehicle airbag, and for the latter, the piston chambers in an engine.

In computer simulations, the structure surfaces enclosing the gas are usually discretized into triangular or quadrilateral patches. During an analysis, either a pre-defined function of time or a pressure/volume gas law usually determines the gas pressures exerted on these patches. The pre-defined function approach involves predicting the chamber volume change *a priori,* and often does not reflect the interaction between the structure and the gas. The gas law option is usually a more desirable approach, since it updates the current chamber volume continuously, and thus takes the evolving structural deformation into account.

In an explicit finite-element code like DYNA3D, because of its inherent limitation on time-integration step size, efficient algorithms for updating the chamber volume are essential to the gas law approach.

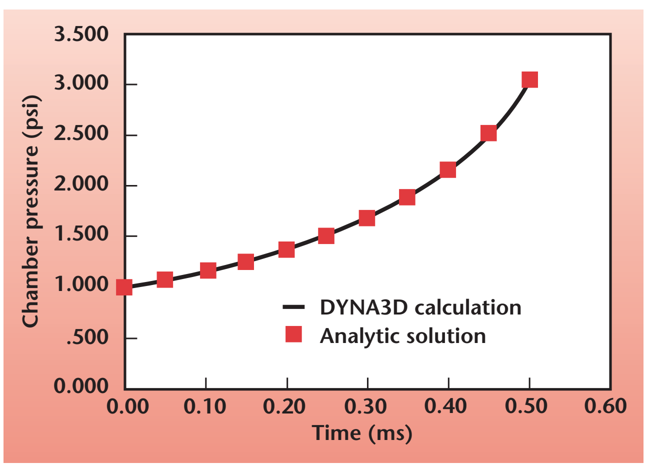

Pressure-time history of a rigid piston suppressing a rigid chamber.

The use of the Divergence Theorem of Gauss with properly selected projection plane attains this goal. The new algorithm hinges on the quick calculation of the volumes of truncated triangular prisms formed by the triangular patches that define the closed chamber and their projections on a common plane. The common projection plane is chosen such that the volume calculation for the truncated prisms is trivial. By orienting the triangular patches so that their normal vectors all point outward from the closed chamber, the chamber volume can be quickly obtained by summing the volumes of all truncated prisms.

In structural analysis, symmetry conditions are often used to reduce the size of the model. The plane of symmetry may cut through a closed chamber in which the gas pressure is present. In this situation, the chamber would appear open because of the lack of discretized patches on the plane of symmetry to close it. The new feature takes this into consideration and overcomes it by selecting a projection plane coincident or perpendicular to the plane of symmetry.

The closed chamber, such as an airbag, is defined by the same set of patches, whereas a piston chamber can be defined by different sets of patches depending upon the position of the piston. When the piston motion suppresses the piston chamber, the chamber will be enclosed by fewer patches, since some of the patches originally in the list will be entirely covered by the piston.

These piston-covered patches may later become active again as the piston moves away. A technique of adaptively tracking the patches defining the piston chamber is accomplished by the use of a reference plane moving in the direction of the piston motion.

A rigid piston suppressing a rigid chamber filled with ideal gas at a constant velocity is used as a benchmark problem because of the available analytical solution. The plot in the figure demonstrates the effectiveness of this new feature in DYNA3D.

Theoretical Model for the EM Effects Induced by High-Energy Photons in Dielectric Materials and Electronic Systems

J. H. Yee, D. J. Mayhall, M. F. Bland

We constructed a model that includes the equations that describe the physics of the recombination and generation of electron-hole pairs by the high-energy photons in the dielectric materials, Compton electron generation rates, and Maxwell's equations.

When a beam of gamma photons penetrates a transmission line or cables, energetic electrons and holes (carriers) are created in the metals and dielectrics of the system by the Compton and photoelectric effects. Through the interaction of the high-energy electrons with the atoms in the solids, many low-energy holes and electrons are created. Since the density of the solids is very high, the mean free path of the high-energy electrons is very short (yielding a time constant of picoseconds or less).

Since electronic systems typically do not respond in such a short time, we can make the approximation that the number of low-energy carriers can be determined by energy deposition by the gamma photons, with the use of a Monte Carlo code. We then divide the deposited energy by the average amount of energy necessary to create an electron-hole pair. To investigate how the EM wave is created by the gamma photons and its behavior as it propagates through the electronic system, we have considered the various recombination and trapping processes of the electrons and holes in the dielectric material.

We modified an implicit, 2-D, finite-difference, time-domain, EM, electron fluid computer code for the propagation of transverse EM (TEM) and transverse magnetic (TM) modes in a parallel plate transmission line in a rectangular geometry, with pressure-variable air as the dielectric material.

To model a coaxial cable to first order in two dimensions, we have also implemented a radial geometry code with two different solid dielectrics between a cylindrical center conductor and an annular outer shield conductor. Both conductors are presently considered to be perfectly electrically conducting.

The first problem that we considered for the gamma radiation effects is for a coaxial cable. We obtained EM wave propagation for gamma ray illumination about the axial mid-point of a two-dielectric coaxial cable model with a step pulse in time, with a strong Gaussian distribution in the axial direction and gamma attenuation in the negative radial direction.

Figure 1 is a surface plot of the E-field generated by the gamma near the axial midpoint of the two-dielectric coaxial cable at 1 x 10^{-16} s. The cable is 0.531 m long and 0.0568 cm at the outer dielectric radius. The discontinuity in the peak E_r indicates the radial discontinuity in the dielectric constant. Figure 2 is a surface plot of E_r at 1.5 x 10^{-9} s. Two wave peaks at r = 0.0346 cm are seen moving toward the ends of the coaxial cable at z = 0 and z = 0.531 m. The peak E_r occurs near dielectric interface at the axial midpoint.

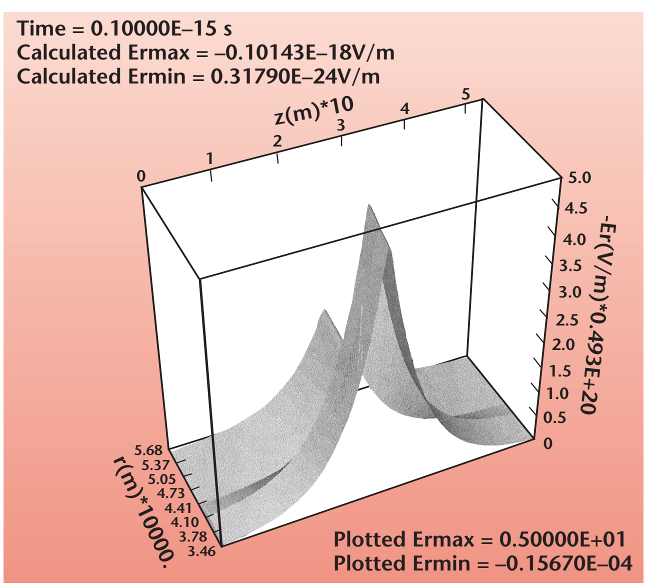

Figure 1. *Surface plot of the E_r field generated by the gamma near the axial midpoint of the two-dielectric coaxial cable at 1 x 10^{-16} s.*

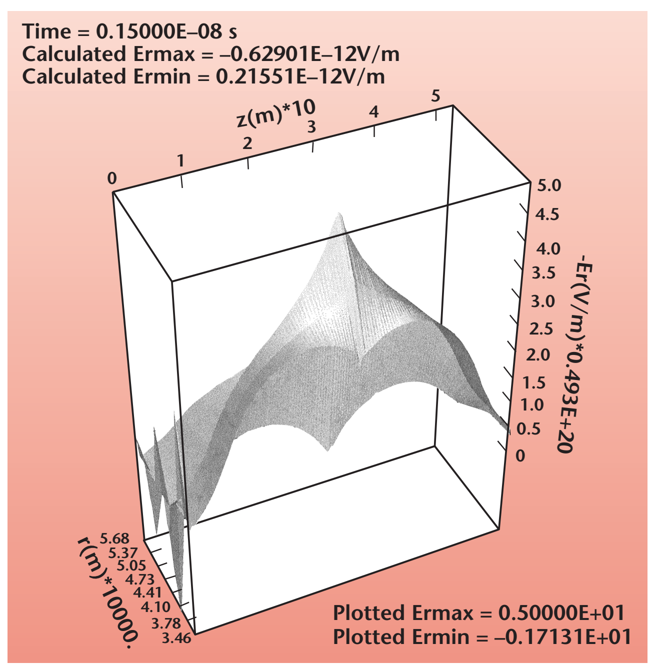

Figure 2. *Surface plot of the E_r of the two-dielectric coaxial cable at 1.5 x 10^{-9} s.*

Center for Microtechnology

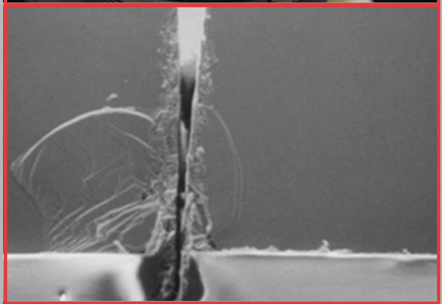

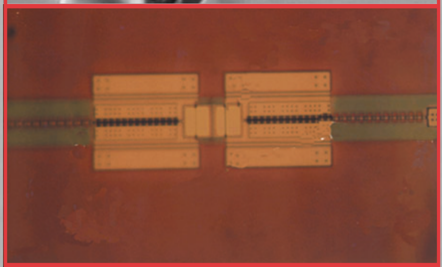

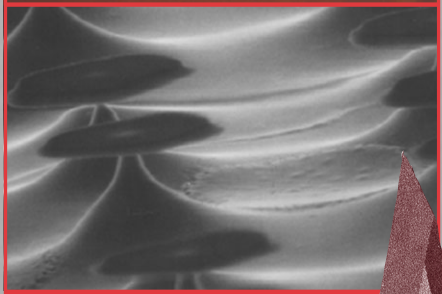

Detector for High-Energy-Density and Inertial Confinement Fusion Diagnostics

J. D. Morse, M. Pocha, J. Kotovsky, E. Behymer, C. Yu, T. Perry; K. Lui (Bechtel, Nevada)

Advanced diagnostics for HED and ICF applications will require detectors sensitive to the 10- to 20-KeV x-ray spectrum. These detectors will make up an imaging array, which is then coupled to a streak camera. We are using the concept of a solid-state x-ray detector, with a field-emission cathode to convert electron-hole pairs generated by the absorbed x rays into electrons emitted into vacuum. Our focus this year has been the suitable detector design and material, demonstration of field emission on the basic platform, and process integration of the field-emission cathode and x-ray detector into this common platform.

A GaAs PIN photodiode has been identified as the nominal solid-state device to achieve both high sensitivity to x-ray photons in the 10- to 20-KeV range, and the temporal resolution requirements for monitoring the time response with acceptable signal-to-noise ratio.

The initial detectors fabricated were PIN photodiodes having a low-doped p layer approximately 4 µm thick. This thickness represents about 8% internal quantum efficiency for the x-ray photon energy of interest for HED and ICF applications. The final design would increase the thickness to match the desired time response (~10 ps/µm): ~50 µm. Additional designs will lead toward gated FEAs for further control of linearity and dynamic range.

One key element in the x-ray cathode design is a high-voltage PIN diode design having low leakage current under reverse bias with no photon signal. For effective photodiode and photon-to-electron conversion, a high electric field must be sustained in the depletion region of the GaAs diode between the N+ and P+ contact electrodes. This is critically dependent on diode fabrication design, to maintain uniform electric field distribution as the charge is depleted in the P-region. In the first run, a planar diode design was fabricated, with the result of very low reverse-breakdown voltage, and high dark current under reverse bias. The subsequent design incorporated a mesa design in the n+ electrode, as illustrated in Fig. 1.

To characterize the electron emission, devices having 200-nm N+ electrode layers were mounted in an ultra-high-vacuum test system at Bechtel, Nevada. A first set of FEA tips formed in an N+ GaAs surface is being tested with a high voltage anode probe. Further tests are underway.

GaAs field-emission cathodes are also being developed to provide another means to convert x-ray photon current into an electron source that can be coupled to an imaging streak camera. Controlled isotropic etching of GaAs is being developed to form uniform arrays of nm-diameter tips (Fig. 2). Subsequent testing in a high-vacuum probe station exhibits >10 µA of field-emission current at 3-kV anode voltage.

These results are a first for LLNL's Microtechnology Center, and further process development will improve the uniformity of the FEAs, and possibly explore low-work-function coatings to improve the emission current.

Next-generation device designs will integrate a gate structure with the field-emission cathode. This will provide an independent electrode to bias the cathode in the linear regime of the field-emission curve, which will, in effect, provide higher linearity and dynamic range.

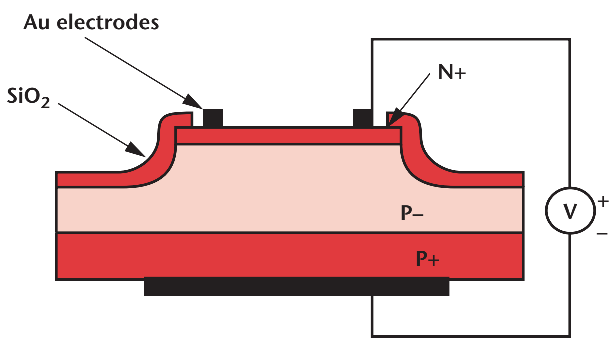

Figure 1. *Cross-sectional schematic of GaAs PIN diode structure with N+ mesa fabrication design.*

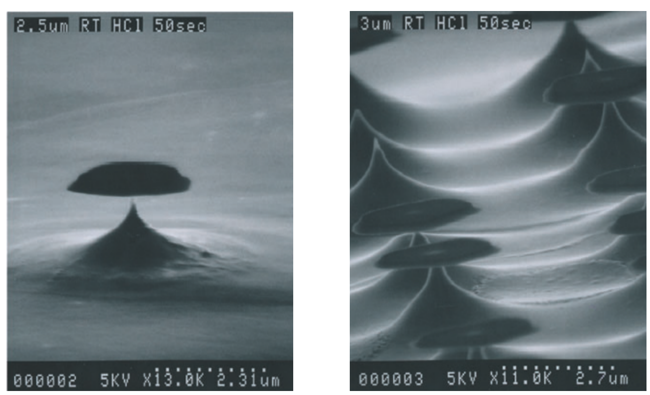

Figure 2. *Ungated GaAs field-emission cathode arrays.*

Fiber Optic Accelerometer

S. Swierkowski, J. Trevino, G. Jacobson, C. McConaghy, A. Throop, C. L. Lee

Miniature accelerometers are broadly useful instrumentation sensors for mechanical systems. Weapons testing needs very small, preferably passive, accelerometers. We have built a 200-g accelerometer, with a footprint of just 4.5 mm x 7 mm, using a fiber optic interferometer readout of proof mass position.

Most commercial devices are large and have electrical power and signal readout; often this is a small signal and the electrical wiring is a hazard in explosive environments.

We have built a 3.5-kHz resonant frequency, 200-g MEMS sensor, using bulk wafer RIE machining, and epoxy packaging. A wafer yield is about 100 parts. The proof mass moves laterally and forms the moving mirror of a Fabry-Perot cavity. The fixed mirror is provided by an optical fiber that is packaged into the 150-µm-square groove in a 400-µm-thick wafer, shown on the right in Fig. 1.

Figure 2 shows the silicon part, epoxy bonded between two glass plates.

The heart of any accelerometer is the proof mass and spring combination (Fig. 3); the resonant frequency determines the bandwidth and the sensitivity of the accelerometer. By adjusting the tether spring thickness a few micrometers with processing, the response of this device can be tuned from about 10 g to 1000 g. Initial testing shows the DC response to be 37 nm/g with 23-µm tethers. A more robust fusion bonded package is desirable for temperature range and stability.

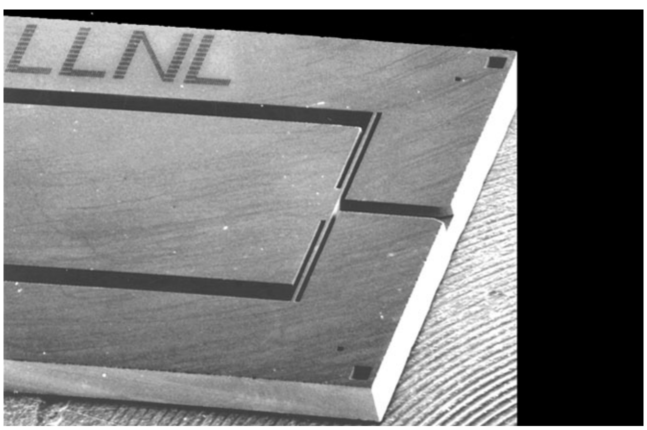

Figure 1. *Key component: the silicon proof mass, with 2 of 4 tethers, 1 mm long, in the frame shown.*

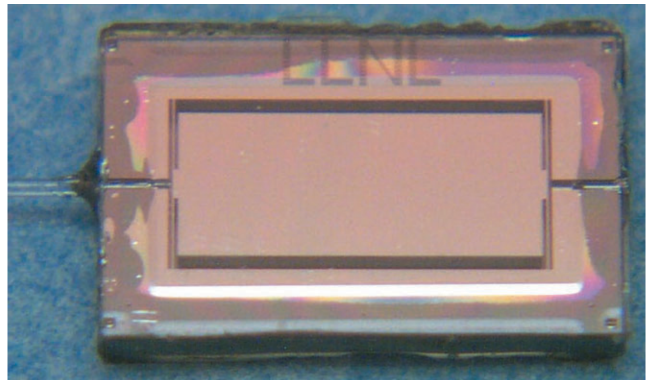

Figure 2. *Silicon part, epoxy bonded between two glass plases, with a multimode optical fiber, to complete the 200-g, 4.5-mm-x-7-mm MEMS accelerometer sensor.*

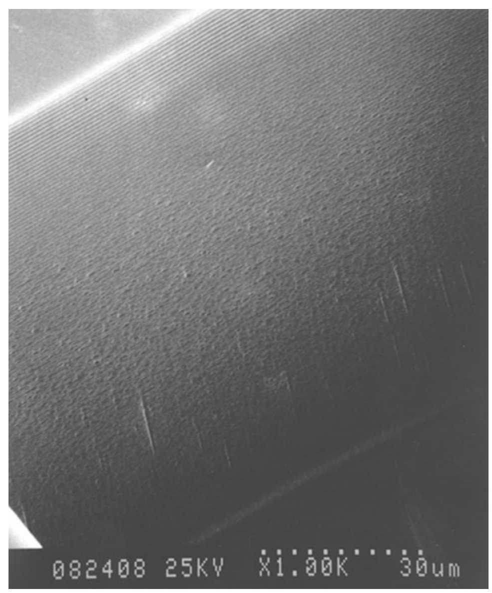

Figure 3. *Silicon proof mass mirror, RIE etched sidewall, smooth enough for the white light interferometer and multimode fiber readout.*

Fiber-Optic MEMS Interconnect and Mirror

S. Swierkowski, J. Kotovsky

During the past year, a 200-g accelerometer has been demonstrated that includes several design, processing, and packaging changes to improve the mechanical robustness, ease of fabrication, and temperature stability. Additionally, 45° mirrors for right-angle optical interconnects have been fabricated and are now in testing.

Significant effort has produced success in packaging the accelerometer in ananodically-bonded high-temperature fusion package. Previous generation sensors were packaged by gluing the three-part, glass-silicon-glass sandwich together. This technique was difficult to fabricate reliably and lacked mechanical robustness. The process was improved by replacing the glue with a fusion bond that hermetically sealed the MEMS device, while maintaining 50-µm alignment and minimizing stress in the proof mass beams. This seal and the internal MEMS components, without the fiber insert (see figure), have been immersion-tested successfully from –196 °C liquid nitrogen to +100 °C water.

Recent versions of the device have attached the optical fiber to the MEMS with a UV-curing adhesive. Control against the adhesive wicking into the sensitive MEMS cavity is achieved through overflow channels, designed for the purpose. Although successful, the fiber attachment process with glue is difficult and tedious because it requires delicate alignment and timing. More importantly, the final positional stability of the fiber is subject to small, slow variations caused by curing and temperature-dependent adhesive properties. To improve this process, a fiber attachment technique with solder has been designed into the next generation of sensors. The attachment technique also includes a self-limiting fiber stop for easier alignment. The new design will offer a more robust and thermally-stable junction of fiber and MEMS. Initial tests with a low-temperature (154 °C) 80 In/15 Pb/5 Ag solder show very strong adhesion to bare glass, polyimide coated fibers, and to Ti/Ni/Au contact pads on silicon.

Several geometry changes have been implemented in the MEMS to improve its performance and to accommodate a wider range of applications. Success of current prototypes has generated interest in versions of the device of varied sensitivity. Continued work optimizes design and processing of the device to improve its mechanical robustness. An improved two-stage plasma etch has been implemented to produce precise mass and spring geometries with much smoother sidewalls for improved mechanical and optical performance. The design has been improved to avoid breakage from shock loading.

Design work for 20-g, 200-g, and 2000-g devices has been completed and is currently in processing. Finally, the sensor size has been reduced by 50% to decrease the cost of manufacture of the device and to improve its function.

A right-angle optical bend has been designed and fabricated. The optical turn is accomplished with a 45° silicon mirror, formed with a plasma-etching process. A package similar to the accelerometer has been produced to pigtail fibers or alternate MOEMS devices to the part. The parts are currently being characterized to determine the coupling loss.

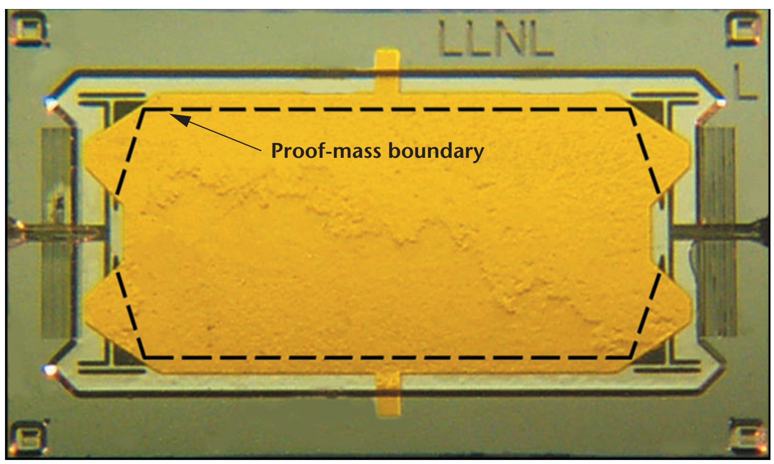

Fusion-bonded 200-g accelerometer with improved bonding, process yield, ruggedness, temperature range, and hermeticity.

Fast-Fiber Multiplexer

M. Pocha, C. McConaghy, T. Bond, T. Lavietes

High-fidelity flight tests required by the Stockpile Stewardship mission demand miniature, minimally invasive sensors to go inside weapons. We have established the Microsensors Program for miniature optical readout sensors. Several different sensors are being developed to measure variables such as acceleration, strain, displacement, pressure, and temperature at various locations within test assemblies.

Sensor measurement techniques are often interferometric, requiring maintenance of coherency of the analog signal between the measurement instrument and the sensor. Space constraints make it almost impossible to bring a bundle of fibers out of a high fidelity assembly. Multiplexing the measurement system is essential to the success of the Microsensor Program.

We have made significant progress, detailed elsewhere. This report summarizes our activities and results for FY02.

We learned that there are a number of applications for compact sensor systems with differing requirements and constraints, which complicates our problem. However, we have identified several potential solutions and are narrowing these down to one or two final candidates. We have also implemented a prototype of one measurement scheme — "In-Phase-and-Quadrature (I/Q)" — that is scalable to smaller size and also allows for multiplexing at least a few sensors in one measurement module.

It became clear that, to meet all requirements, the systems would have to operate within a very severe environment. For example, the full temperature range for weapons grade systems is –65°F to +165°F. Also, components used in many flight tests need to withstand accelerations up to 200 g. There are actually two kinds of measurements that need to be made — absolute and relative; and two ranges of data capture speeds — <100 Hz/channel for most of the parameters being measured (temperature, pressure, strain), and >5 kHz/channel for others (acceleration, and possibly some gap measurements). These demands, along with the multimode analog bandwidth requirement, place severe constraints on any multiplexing scheme.

We learned from our survey that most commercial effort is going into single-mode switching for the telecommunication industry and is not likely to produce components for our needs in the near future. Commercial multiplexers are lacking bi-directionality, or bandwidth, or the speed required for our applications. We continue to follow developments in this fast changing field, but will most likely have to develop our own multiplexing technology.

Of the several technologies that could be used for multiplexing, (MEMS mirrors, liquid crystal, bubble switches, electro-optics, thermo-optics, holographic switches, acousto-optics, spinning mirrors, source switching, interferometric switches), we have narrowed our attention to three areas that are most likely to work for our applications — thermo-optics, source switching, and rotating mirrors.

We have collected a large number of papers on thermo-optic and electro-optic switching, some of which discuss multimode operation. If we can design a scheme that allows us to achieve the switching speeds required with multimode operation, then this technology could make very compact switches that would be relatively easy to fabricate.

The prototype I/Q measurement system we designed this year is compatible with a limited degree of multiplexing, using source switching — a separate optical source (*e.g.*, LED) is connected to each sensor, and multiplexing is done by switching the sources on and off. The readout of the signals from all the sensors can be done in a common, single optical path. The required measurement speed can be achieved, and, although our prototype is a relative measurement system, absolute measurement capability is possible.

Spinning mirrors are multi-faceted mirrors that are mounted on high-speed motors and scan a reflected input beam across the face of several output fibers. High-speed, miniature motors are available that can achieve up to 100,000 rpm in about a 1-cm-long package. These are sufficiently fast to spin a multi-faceted mirror at the speeds needed for 5-kHz multiplexing, but further study is needed to see if a compact lens and optical path can be designed to confine the beams sufficiently for fiber-to-fiber free space multiplexing.

While continuing to follow commercial developments, we recommend that our efforts be focused on the three techniques we have identified as the most promising for the Weapons Program requirements. With further study we expect that one or two of these will clearly stand out as the optimal solution(s) to the multiplexing problem.

Fabrication and Testing of High-Stroke Adaptive Optics Actuator

A. Papavasiliou

The purpose of this project was to build and test a high stroke actuator for use in space telescopes. The unique scissors jack design converts small horizontal displacements into large vertical displacements. Our goal was to reduce this approach to practice.

The specific technology to be incorporated is a MEMS-based actuator for deformable mirrors (DMs) that can be used to correct for aberrations in lightweight space telescopes. These telescopes are under increasingly active investigation to substantially lower costs.

A serious concern with lightweight mirror technologies is how to control their optical quality during both fabrication and deployment, and how to maintain the surface quality on orbit with changing gravitational, centrifugal, and thermal loads. A potential method for correcting aberrations in lightweight space telescope optics is to use a DM to cancel the primary mirror aberrations. As on-orbit changes in the primary mirror occur, the shape of the DM can be readjusted to maintain the correction.

Conventional DMs have many drawbacks — they are expensive, heavy, use significant power, have limited stroke, have limitations on the number of actuators, and do not work in cryogenic environments. MEMS-based adaptive optics (AO) has the potential to address all of these issues.

The goal of achieving a high stroke actuator with 50 µm of vertical displacement was to be accomplished by designing beams that buckle out of the plane of the wafer when they are actuated parallel to the plane of the wafer. To do this, a basic design was worked out that was compatible with a conventional fabrication process.

The design included beams with crenellations engineered to force the beam to buckle in the right direction, electrostatic comb actuators, and stabilizing springs. Two different types of actuator were designed, a two-beam actuator and an eight-beam scissors jack-type actuator.

A computer model was created to describe the predicted performance of the devices. That computer model was then used to find optimal designs. The constraints on the optimal design were the specifications of the fabrication process on film thicknesses and minimum feature sizes and spacings. The optimal criterion was to make the displacement vs. voltage curve have as large a stable region as possible while reaching 50 µm at 100 V.

The optimal designs and a number of other variations were laid out and submitted to the foundry service. A post-processing method was developed to use a SU-8 photo-curable epoxy block as an insulating mechanical connector between the two high-potential sides of the actuator. Two different release processes were investigated to allow the fragile polysilicon parts to be released from the silicon dioxide in which they were fabricated without permanently sticking together. An existing critical point dryer was re-certified, and a process was implemented to coat the chips with a hydrophobic self-assembled monolayer, akin to coating the pieces with a monolayer of Teflon.

Our test results are as follows.

Probe actuation

The devices were pushed horizontally by mechanical probes and reliably translated the horizontal motion to a vertical motion. This showed that many aspects of the design do indeed work properly; the beams buckle in the correct direction, not downward and not sideways; and the SU-8 epoxy insulating connector works.

Electrostatic actuation

We were not able to actuate devices as predicted electrostatically. One actuator did move vertically under electrostatic actuation, but not with the expected mechanism.

Thermal actuation

We were able to actuate a thermal actuator (Figs. 1 and 2). Simplified versions of the actuators were fabricated without electrostatic elements. Current was run through the beams of these devices to heat them. The expansion of the beams moved the actuators. Buckling was observed at 8 mW, and displacements of as high as 9 µm were observed at 35 mW.

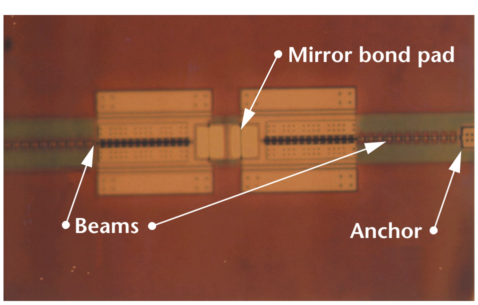

Figure 1. *Photograph of thermal actuator.*

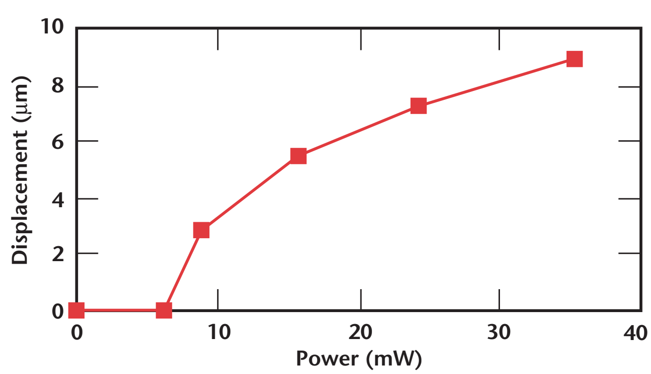

Figure 2. *Plot of thermal actuator displacement data.*

Water Security Microdevices

E. R. Cantwell

The goal of this project was to evaluate new concepts for a device to handle the near-real-time, continuous detection of biological materials in raw water. The acquisition and processing of samples in current technologies present a set of new problems, e.g., biofilms, filtration systems, and low concentrations that can affect human health, when conducted continuously in water. We have developed an in-house base of expertise, such that LLNL now has a credible team for attacking the main problem areas.

Design issues we have dealt with include:

1) continuous feed of water into the system;
2) low concentration of pathogens—the system must sample a large amount of water, and the samples must be concentrated to reduce detection time and increase accuracy;
3) distribution of beads—a bead-based system mitigates the effect of biofouling;
4) contamination threat scenarios.

A system was built to investigate the possibility of using magnetic beads (which would be antibody-coated) to capture pathogens in large volumes of water, then to filter it down to a manageable size. Our five-gallon tank represented an inlet from a lake. Magnetic beads were mixed throughout the volume using a stream of compressed air. We pumped the beads into a series of pipes ranging from 1.25-in. ID to 0.25-in. ID. Magnets were placed external to the pipe to collect the beads.

The hope was to provide enough magnetic force to move the beads to the side of the tube to fractionate the liquid, but invariably beads would accumulate, particularly in areas where discontinuities in the pipe caused eddy flows. The accumulated beads naturally focused the magnetic field, inducing further accumulation. Thus, this technique was more appropriate for capture and release methods of concentration even on this scale.

Magnetic beads are not necessarily attractive for DNA assays, so a large filter capture system was built for polystyrene bead capture. Filters do not return all beads, but they are inexpensive and be easily replaced.

A flow-through dielectrophoresis (DEP) device was being built. Good side-wall electrodes were difficult to fabricate. Experiments indicated that much higher voltage could be used than had been used previously, thereby reducing the restriction on channel width from 25 µm to nearly 500 µm. A larger channel will make the fabrication of side-wall electrodes easier. The advantage to DEP focusing is the elimination of beads.

This project has several sources of funding:

- Funding from the US Bureau of Reclamation to do water security studies of dams and reservoirs.
- New funding from the SFPUC to do the same sort of studies for San Francisco.
- Negotiations between LLNL and LA Metropolitan Water for laboratory methods for detecting biological WMD materials.
- Chem-Bio Nonproliferation Program (CBNP) proposals to DoD that are pending. CBNP is also looking at extending the Advanced Particle Detection System capability to water by adding a new “front-end” that will do extractions from raw water. This work would be dependent on next year’s funding, which is unknown at this date.
- New technology-base proposal based on discussions and meetings with the Joint Services Water Monitoring program at Edgewood Chemical and Biological Center, part of the Army's Aberdeen Proving Ground in Maryland.

Although we did not achieve our goal of demonstrating a prototype device, all involved acknowledge that the problems we propose to solve are significant and that we have a head start over many others doing research in this area.

This work has also served to convince NAI and Energy & Environment that water security is an arena in which LLNL can make a difference. NAI has co-sponsored several high level speakers to give talks on water security and biological detection, and has verbally supported a technology-base proposal that is an outgrowth of this work. Energy & Environment is nearing the point of announcing their Water “Grand Challenge,” and again, water security is likely to play a significant role in this plan, in part due to input on technology from the investigators in this project.

Portable Bioanalysis Instrument with Integrated Sample Preparation and Detection

P. Krulevitch, M. Bennett, J. Dzenitis

We are designing microfabricated systems for preparing biological samples for immunological and genetic assays. We investigated alternative miniature and robust detection strategies that can be integrated with our sample preparation modules.

While sample preparation is one element of a portable bioanalysis instrument, new detection methods must also be designed. The accepted techniques – flow cytometry and the polymerase chain reaction (PCR) – suffer from several drawbacks that prevent miniaturization and portability.

Flow cytometers, which are large, delicate, and alignment-sensitive, use large volumes of sheathing fluid to precisely position particles for individual confocal detection. Instrumentation for PCR-based DNA amplification and detection can be miniaturized, but automated sample handling and the ability to run multiplexed assays remain elusive.

In this project, we investigated alternative miniature and robust detection strategies that can be integrated with our sample preparation modules to create portable bio-detection instrumentation for counter biowarfare and biomedical applications. M. Bennett, from LLNL's Biology and Biotechnology Research Program, worked closely with our microfabrication group to quantify the effectiveness of sample preparation and detection methods.

We investigated the use of microchip-based capillary electrophoresis (CE) for DNA sequence detection. Real-time fluorescence monitoring of PCR, the current approach used by LLNL for rapid, DNA-based bio-detection in the field, is limited in its ability to screen for multiple agents simultaneously.

In our work, PCR is used to amplify specific sequences of interest if they are present, and CE is then used to detect and identify the amplicons by size. This approach lends itself to both multiplexing and miniaturization. We ran multiplexed PCR with new fluorescently labeled primers and demonstrated amplification of different bacterial bio-warfare surrogates by running standard agarose gels. To demonstrate our ability to run this assay in a capillary/microchannel format, we performed separations using a commercial CE sequencer (ABI Prism 310) and saw that we could identify the amplicons in the resulting fluorescent electropherogram (see figure).

Recently, we have been working with a microchip-based CE platform that, with the incorporation of compact optics, electronics, power, and packaging, has the potential for miniaturization. We have been successful in showing signal differences between a singleplex PCR solution with and without amplification, and are working toward a demonstration of multiplex detection and identification.

DNA purification and concentration using microfabricated chips was investigated as a sample-preparation front-end for microchip capillary electrophoresis. *Erwinia herbicola* DNA samples were mixed with a chaotropic salt solution (pH 5.3), which lysed the bacterial cells, and the resulting solution was applied to the DNA extraction chip. This solution contained both the nucleic acids in which we were interested, along with detritus from the lysing process.The components of the lysing solution that were trapped on the purification chip were washed with 70% EtOH and air-dried. Ten mM Tris (pH 8.5) was applied, the devices were warmed to 72 °C, and this concentrated, purified sample was eluted as single 20-μl drops. This procedure was established elsewhere, to separate, purify, and concentrate the nucleic acids as preparation for PCR. Real time PCR was then performed to determine capture and concentration efficiency. Results showed a 12-fold concentration using the chip-based pre-concentration. A design for a miniature, automated instrument for performing the DNA concentration and purification process was submitted for funding to the DOE Chem-Bio Nonproliferation Program. The work performed through this project seeded several new efforts aimed at portable bio-detection instrumentation. Our concept for a fieldable microfluidic system for nanoparticle-based bioassays was submitted to the National Cancer Institute. Our proposal to develop a multiplex portable bioanalysis instrument for detecting biological warfare agents was accepted as a new LDRD ER FY03 project. We submitted a FY03 proposal with Sandia National Laboratory to DOE for the BioBriefcase, a portable bioagent detector.

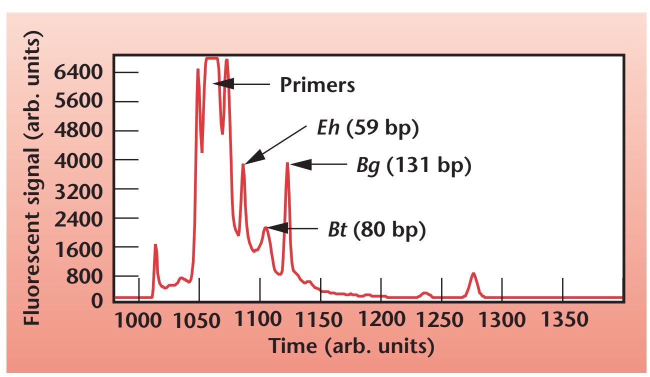

Electropherogram of a PCR solution, showing identification of three pathogen surrogates (Erwinia herbicola (Eh), Bacillus thuringiensis (Bt), and Bacillus globigii (Bg)).

Three-Dimensional Microlithography System (3D-MLS)

V. Malba, A. F. Bernhardt, L. Evans

We have initiated the upgrade of an existing Laser Pantography system by installing new motion control hardware and software, and interconnecting them with an existing set of precision stages.

A decade ago, LLNL's Microelectronics Program developed a unique quasi-3-D laser direct writing tool, called Laser Pantography, to fabricate metal interconnects on multichip modules. The program also developed a suite of processes for deposition, etching, and lithographic patterning of 3-D surfaces. In addition to the multichip modules for which the system was created, this tool and the associated processes allowed the program to make unique millimeter- and submillimeter-scale parts such as RF inductors, diamond anvils with electrode structures, NMR microcoils, micromotor stators, and magnetic relays.

The Laser Pantography tool had fundamental limitations, however, and because of the original mulitchip module application and limitations in the CAD/CAM systems of the time, the configuration could not support out-of-plane patterns more complicated than straight lines of fixed length parallel to the z-axis. Also, the workstation was out-of-date, using an operating system no longer supported.

Another limitation was that motors could not be started at exactly the same time. This meant that diagonal lines in the x-y plane, to use a simple example, were executed as stair steps. A modern motor control system would allow simultaneous movement of multiple stages so that smooth diagonals, ovals, and other shapes could be drawn.

The limitations have been addressed in this TechBase project.

We have begun the assembly of a modern, fully 3-D, sub-μm-accuracy motion system driven by a commercial CAD/CAM package. This 3-D Microlithography System (3D MLS) functions as a five-axis milling machine with a focused laser as the "cutting tool."

With improvements in the optical system, the "cut size" can be 1 µm. The upgrade of the 3D MLS will involve the replacement of the original custom hardware and software with a standard motion control hardware package, together with commercially available 3-D CAD/CAM software, which is licensed to LLNL. The new software will output standard G-code, which the new hardware will be able to execute in the same fashion as a five-axis CNC milling machine.

A true 3-D Microlithography System will be the final product. It will be a unique capability, and is expected to generate considerable interest and funding. It will dramatically increase the 3-D patterning capability of the present system, making it more applicable to surfaces and structures, which cannot now be patterned. As technology demonstrations, we will pattern helices on < 400-µm-diameter cylindrical surfaces (for NMR and MRI applications) and simple periodic structures on spherical or elliptical surfaces of radius of order 1 mm (for NIF physics targets).

In FY-02 we installed new motion-control hardware, including a Pentium computer, a Delta Tau microprocessor control card (PMAC card), motor amplifiers and motor controllers for up to eight degrees of freedom. A 3-D, CAD/CAM package has been installed, and initial handshaking software linking it to the motion control hardware is in place. X, y and z translation stages (existing equipment) have been installed and wired. Requirements for high-precision theta motion in x and z axes have been ascertained, and stages with sufficient speed and precision have been identified for purchase. A high-power UV argon-ion laser was procured internally and is being refurbished. An optical design emphasizing a small focal spot, which can be expanded for rapid patterning of large areas, has been completed, and the required components identified. Advances in all-quartz microscope objectives now permit deep sub-µm resolution at the UV wavelengths we use.

In the coming year we will complete the motion system with two rotation stages. We will also complete a system motion mapping capability for obtaining high-accuracy motion and we will characterize system performance. We will assemble a new optical system (objectives, tube lenses) designed for versatility as well as minimum feature size under various motions.

A kinematic mounting scheme is envisioned for smaller parts and for rigid parts. This scheme will be our focus in the third year of the TechBase project.

Gallium-Arsenide Cutting Techniques

G. Cooper, G. Jacobson, S. Oberhelman, M. Shirk, T. Hauck, N. Raley

High-voltage components, including photovoltaic circuits, invariably have to contend with electrical leakage and arcing through gases, along surfaces, and through solids. Recent test results on arrays of photocells fabricated as monolithic, integrated circuits have revealed the presence of undesirable currents flowing through the solid substrate from areas of high potential to areas of low potential. The devices were designed and fabricated with special layers between the photocells and the underlying substrate to reduce or prevent such currents from flowing in the substrate. The goal of this project was to investigate techniques to isolate the high- and low-potential areas of the array from each other while parallel work is done to analyze the mechanisms of the current leakage and identify integrated solutions.

One of the problems inherent in the design of high-efficiency photocells is the substrate requirement. Gallium arsenide (GaAs) is the semiconductor of choice for producing the most electrical power from a given optical collection area and fixed illumination. Unfortunately, as a substrate, GaAs is not a good insulator.

One technique to keep electrical charges from flowing through the substrate is to physically partition the substrate into isolated islands. Because there will be many small islands produced in a high-voltage array, individual handling of each island should be avoided.

The isolation concept examined by this work is to permanently bond the GaAs substrate (upon which the photovoltaic array is fabricated) to an appropriate insulating substrate. GaAs material is removed between the islands all the way down to the insulating substrate. The islands thus become electrically isolated from each other by the channels, but the array may still be handled as a single component.

Two existing processes at LLNL were examined for functionality, repeatability, and simplicity: saw cutting and femtosecond (fs) laser ablation. The common issues are: minimal achievable width of cut, lateral extent of collateral damage, redeposition of material on wafer surface, mechanical retention of separated islands, cracking, and complete removal of the GaAs material between islands.

Samples for each technique were prepared by adhesively bonding 20-mm -x- 20-mm pieces of 350-µm-thick GaAs to 1-mm-thick pieces of glass. Permabond 910 cyanoacrylate was used for the initial tests because of past favorable experience and ease of handling.

Sawing, using an older model semiconductor wafer saw that has been adapted for use with hazardous materials, has demonstrated promising results. Of the available blades, the 0.8-mil thickness with 4- to 6-µm grit appears to produce a cut of 90-µm width, including minimal chipping (Fig. 1).

Paradoxically, the 0.6-mm-width blade produces more chipping and a more extended damage width. Parallel cuts at a pitch of 500 µm did result in debonding of the GaAs island between the cuts. This was probably a result of mechanical vibrations and the crystalline nature of the Permabond adhesive. Samples were prepared using an alternative UV curing adhesive, but have not yet been cut with the wafer saw.

Removing material with a fs pulsed laser has also produced favorable results. The laser used for these experiments produces 150-fs-width pulses at an energy between 25 µJ and 250 µJ per pulse, and a repetition rate of 1000 pulses/s at a wavelength of 820 nm. The beam is focused to a spot size of 45-µm diameter on the GaAs surface inside of a vacuum chamber. The beam is rastered back and forth across the channel that is to be removed between the islands, removing a thin layer of GaAs with each pass. Figure 2 shows a magnified view of an 80-µm-wide channel using optimized cutting parameters. Complete removal of the GaAs in the channel has been achieved with minimal redeposition. We have not seen any debonding of GaAs between channels using this technique.

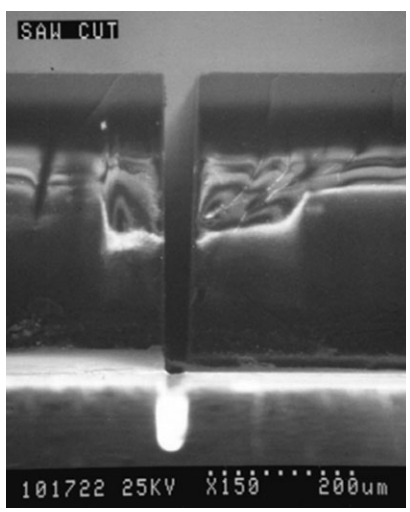

Figure 1. *SEM micrograph of profile of saw-cut channel through GaAs substrate into glass plate below.*

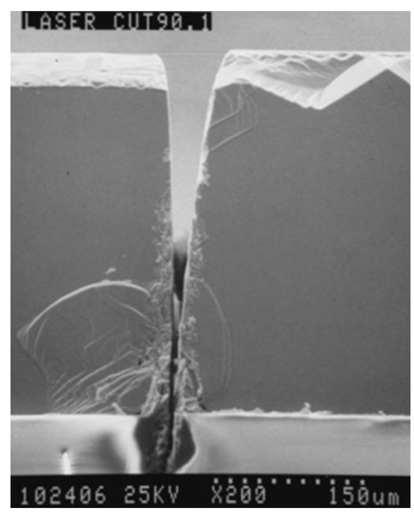

Figure 2. *SEM micrograph of profile of laser-cut channel through GaAs substrate into glass plate below.*

Nucleic Acid Sample Preparation Methods

K. Ness, S. Lehew

The objective of this work is to demonstrate rapid and effective extraction and concentration of DNA from solution using a micromachined high-surface-area silicon chip.

In our approach (Fig. 1) we replace the glass beads in the traditional "Boom" purification method with an array of silicon micro-pillars. The MEMS-based DNA pillar chip structure offers a high surface area (~25-fold increase); a low liquid volume (~2 μl); integrated thermal control; and reproducible fluid flow fields to provide efficient capture and release of DNA in a flow-through system.

Results show the DNA pillar chip is able to concentrate and purify DNA in about 10 min.

Figure 2 displays the results from real-time PCR used to quantify the DNA pillar chip performance. Over 1000-fold increase in concentration and removal of PCR inhibitors from the sample are seen with the pillar chip.

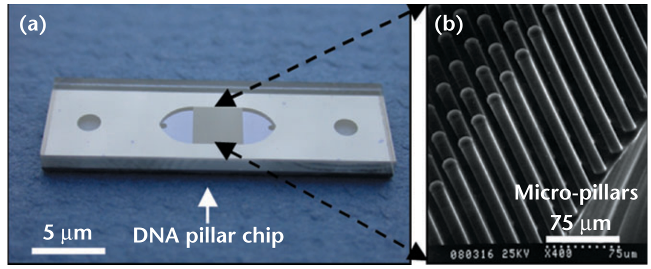

Figure 1. *(a) DNA pillar chip: array of 30,000 micro-pillars (gray region in center of chip); (b) SEM of micro-pillars (diameter x height : 5 µm x 225 µm).*

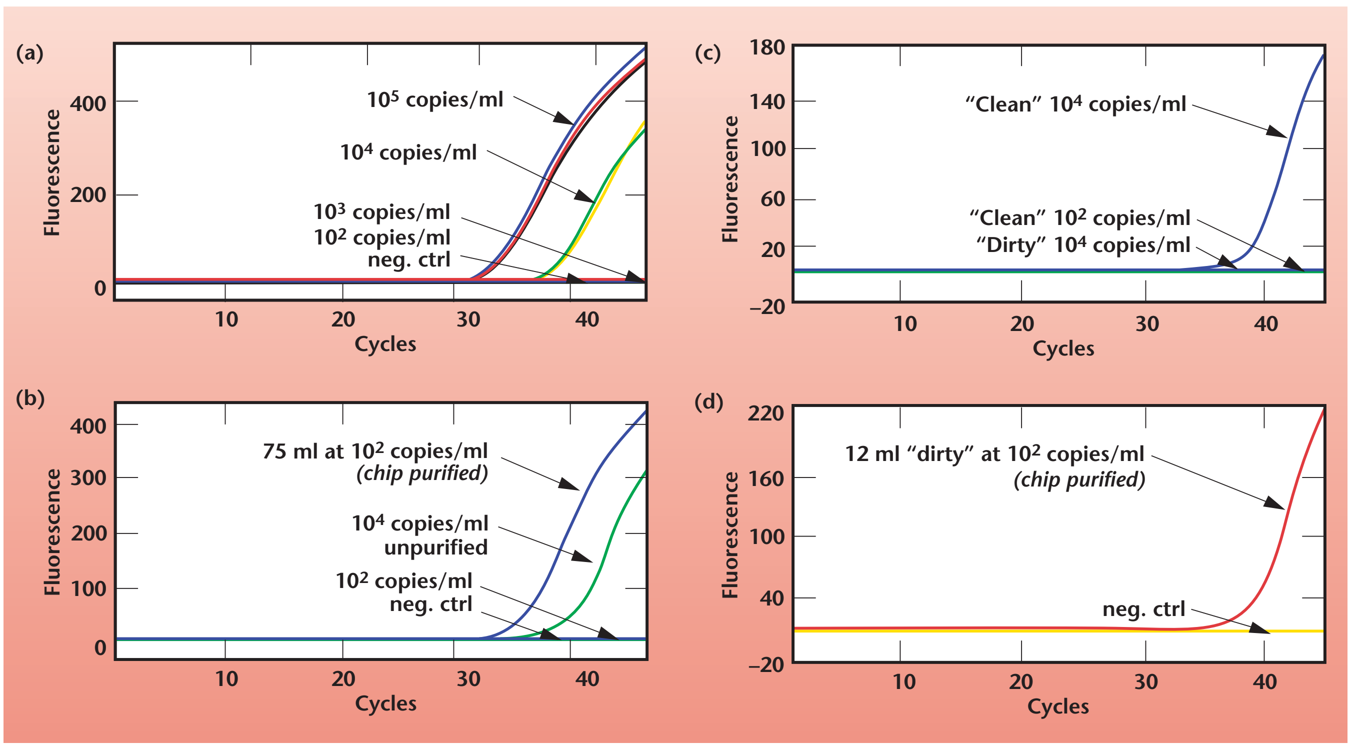

Figure 2. *(a) Standard taqman curves for Francisella tularensis: starting samples 10^2 – 10^5 DNA copies/ml; (b) 1000-fold concentration: 10^2 DNA copies/ml concentrated to 10^5 DNA copies/ml using large volumes (75 ml); (c) PCR inhibition studies demonstrating "dirty" water sample is inhibitory in nature at a concentration of 10^4 DNA copies/ml; (d) extraction of DNA from "dirty" water sample showing purification using the DNA pillar chip.*

Miniature Aerosol Collector

D. Masquelier

The objective of our experiments was to evaluate the physical particle collection efficiency of our prototype aerosol collector. The design was evaluated at a slightly larger scale than the ultimate construction, but it allowed the concept to be thoroughly explored and any challenges to be examined.

The first step in any system for detection and characterization of biological agents is a sample collector. This can take on the simple form of a cotton swab for solid surfaces, or as in the case of airborne pathogens, an aerosol sample collector to collect and concentrate airborne particulate onto a filter medium, or into a liquid sample volume for subsequent preparation and analysis.

An aerosol sampler is the most appropriate for continuous monitoring scenarios, where repeated swabbing of settled particles is impractical. Most commercial samplers now available for field use are large, power-consuming, and produce collected sample into large volumes of liquid, typically >30 mL. Emerging miniature detection systems analyze much smaller sample volumes, typically <250 µL. When using the currently available air samplers, the sample volume must be "sub-sampled," effectively diluting the sample, resulting in a loss of sensitivity of detection.

This project explored a new concept to collect particulate at a relatively high air-flow rate, and yet designed so that the resultant delivered liquid volume would be only 200 µL or less. This would address the problem of dilution because of sub-sampling. The size, weight, and low-power specifications of this aerosol sampler would ultimately need to closely match the current state of the art in pathogen detection systems, which would greatly ease the deployment in remote locations.

We have tested an alpha prototype of a working collector. Figure 1 shows the assembled collector "piggy-backed" onto a modified vacuum cleaner that served as an ideal test-bed fixture and an air-flow source.

Figure 1. *Prototype of a working collector.*

The test system for the determination of the particle collection efficiency is shown schematically in Fig. 2. In several of the experiments an optical particle counter was used in parallel to the Aerosizer (not shown). Using the particle size distribution data measured upstream and downstream of the collector, the collection efficiency was determined by:

Overall Collection Efficiency = $(1 - C_{DOWN}/C_{UP}) \times 100\%$

Typical experimental results (Fig. 3) measured collection efficiencies between 35 to >95% for particulate sizes between 0.5 to 1.5 µm into liquid volumes of 2 mL, at airflow rates up to 275 L/min.

A "path forward" plan has been initiated to continue this effort and scale down to the final dimensions. A patent application has been submitted based on this work.

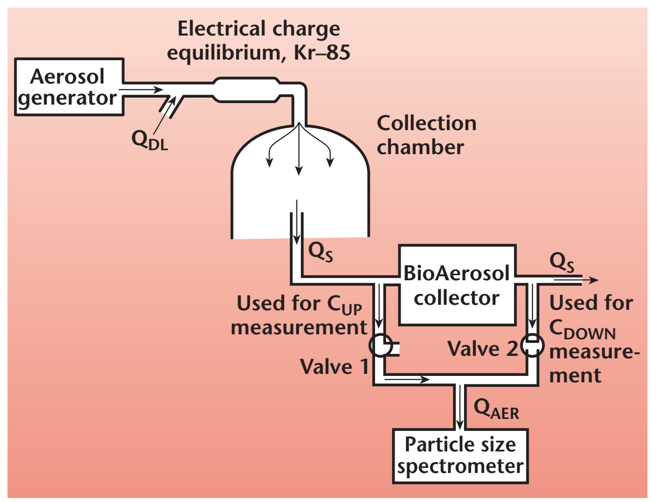

Figure 2. *Test system for the determination of the particle collection efficiency.*

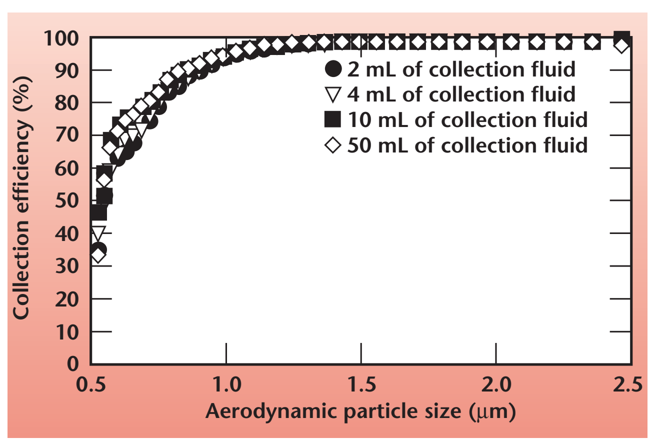

Figure 3. *Overall collection efficiency when collecting polydispersed oleic acid particles at 275 L/min.*

Center for Nondestructive Characterization

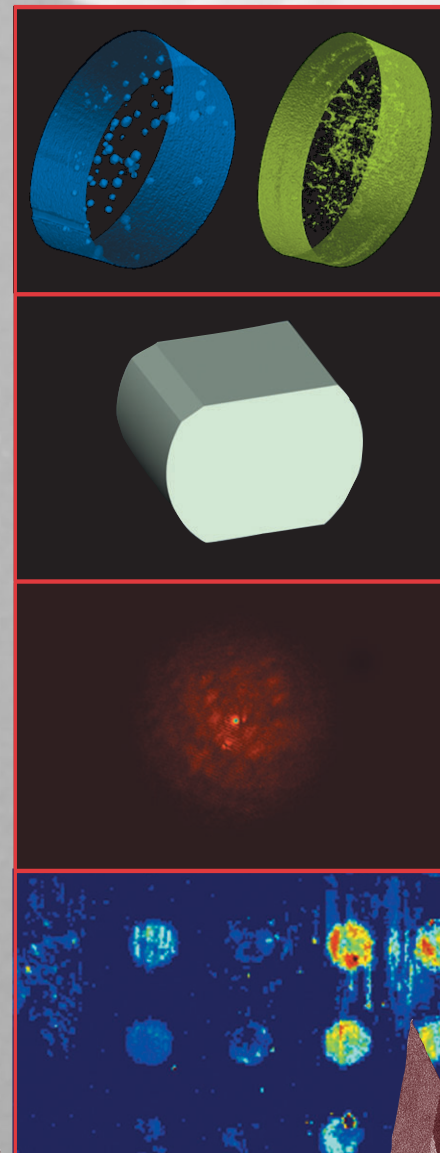

Feldkamp X-Ray Tomographic Reconstruction Algorithm on a Distributed Computer System

H. Jones, D. Barker, M. Kartz, P. Roberson, P. Schaich, Y.-M. Wang

A parallel Feldkamp tomographic reconstruction code is needed at LLNL to reconstruct CT volumes of unprecedented scale, varying from 2k x 2k x 2k to 8k x 8k x 8k (32 GB to 2048 GB). This follows the trend in CT detector technology that ranges from 3k x 2k (current) to 8k x 8k pixels (near future). This implementation encompasses a small segment of a much larger infrastructure requirement to deal with enormous NDE volume data sets, including postprocessing and visualization. This project was successful at developing a foundation for the methodology and techniques used to port an existing code into a parallel execution framework.

A portion of this project evaluated the efficacy of porting and running parallel Feldkamp on existing LLNL ASCI computer resources, while maintaining the design philosophy of low memory footprint, limited internode communication bandwidth, automated resource discovery, a worst-case execution time of 24 h maintained across problem sizes, and *in-situ* postprocessing analysis.

An existing LLNL NDE cone-beam tomographic code was modified to port easily to many parallel architectures, including Linux-PC, Compaq Clusters (GPS and TC2K), and ASCI Blue. Internode communications are MPI-based. Code additions include Node/Memory resource discovery, modified File I/O to accommodate NFS or GFS (networked file systems), distributed reconstruction volume and I/O, and a communication mechanism to interchange projections (the input data set).

The first phase was concerned with feasibility studies on parallelizing the Feldkamp (fkrecl) and Convolution Back Projection (CBP) NDE codes. A small PC-based cluster was put together for the initial implementation.

The second phase was to design for low memory footprint and port to LLNL ASCI machines. In addition to the Linux NDE cluster and GPS, the algorithm was successfully exercised on 100 nodes of ASCI TC2K (see figure).

The formula for the Feldkamp, Davis, & Kress (FDK) algorithm may be analyzed for scalability and used to predict execution times as the problem's size and/or number of processors is varied.

The parallel Feldkamp project was successfully implemented and demonstrated to run on a variety of architectures using up to 100 processors. An expanded version of this report includes details on porting issues, example usage on various platforms, and implementation.

Next, the communications scaling should be analyzed when the execution environment involves thousands of processors. *In-situ* postprocessing of the reconstruction volume should also be considered. The inner loop memory access patterns should be analyzed at all levels of the processor memory hierarchy. Also, before a large production effort, a sensitivity analysis should be done on the core numerics over a range of cone angles, sensor characteristics, and acquisition geometry, to better understand the limitations of the algorithm.

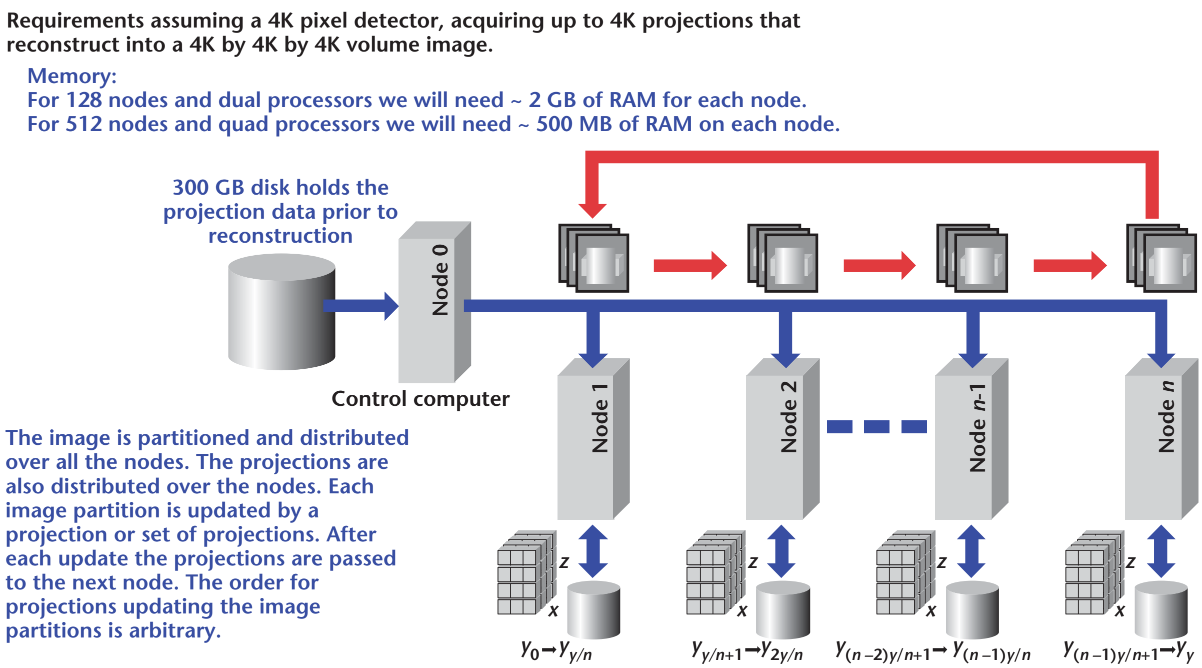

Diagram illustrating data partitioning and flow during reconstruction.

Three-Dimensional Rendering of High-Frequency Ultrasonic Data

G. Thomas, S. Benson

This project is evaluating techniques to render ultrasonic nondestructive evaluation data in three dimensions, thus greatly increasing our ability to interpret data.

Traditional ultrasonic imaging converts amplitude-time information into a 2-D image by time-gating the data and color-coding the amplitude of the signal in the gate. Unfortunately, this approach throws away the depth information. We are capturing all the information in the ultrasonic waveform and processing that information to generate a 3-D image.

Once the image is rendered, it can be manipulated to best display the internal structure of a component. Thus, 3-D rendering of ultrasonic images greatly increases our ability to interpret the data. Our customers gain a better understanding of the results when viewed in three dimensions. Also, our ability to characterize components in three dimensions will support modeling of the parts.

There are two main tasks involved in rendering ultrasonic data in three dimensions. One task is to capture the full ultrasonic data set and store the data in the computer. The other main task is processing the data to render the 3-D image.

Our progress to date includes specifying and acquiring a software package that renders data in three dimensions. We selected a software package called Terra Recon, which generates 3-D images and manipulates the images to improve visualization of internal structure. We learned to operate the software first on a set of x-ray computed tomography data, and then on a set of model-generated ultrasonic data. We do not have real ultrasonic data sets yet.

We are presently configuring the electronics and writing software to acquire real ultrasonic data. Capturing the full ultrasonic waveform entails assembling the instrumentation and writing the computer drivers to digitize the signals. These signals must be correlated to the scanner position at the time of digitization. Once the ultrasonic data has been stored, computer programs convert the large data set of full waveforms into a volumetric display. These conversion codes need to be written.

This display can be manipulated to best show defects and other characteristics of the inspected components. These tasks will be completed next year.

The final product will be a technology to capture and render ultrasonic data so that 3-D characterization can be realized. This information can be incorporated into modeling codes to predict component performance based on as-built characteristics.

Application of Photothermal NDE to Large-Scale Optics

R. Huber, D. Chinn, C. Stolz

A photothermal system built during FY01 was modified to allow faster data acquisition.

The major modifications to the photothermal system involved changing from a camera with slow readout to one with a faster readout, and the specification and incorporation of a long-working-distance microscope lens. The camera readout has been reduced from around 40 s to less than 8 s, a considerable decrease. The new lens allows a field of view ranging from around 200 µm to several mm. Also, major modifications were made to the control software to allow for the new camera, and to complete scans.

The major difficulties encountered during this work dealt with finding and mitigating the various sources of noise in the images. Primary among these noises were fringes that did not subtract out in the images. Several sources for these fringes were found, including two glass covers on the CCD camera.

Another problem is associated with the probe laser that is used to produce the images. Tiny variations in intensity and pointing stability become significant since we are operating with short exposures and very small field of view. Also, the mounting of the probe laser and lens/camera combination was found to give problems—any motion of these components can produce errors, because this technique uses image subtraction. If there is motion between the images to be subtracted, this will add to the noise in the final images and possibly obscure the data.

Even though there were numerous difficulties encountered during the course of the year, significant progress was made and the current system is up and running. The figure shows a bright spot associated with an absorber on a BK7 glass sample. This particular image has tremendous signal-to-noise, but suffers somewhat from the fringes mentioned above.

There is still room for improvement to make this system robust and more sensitive. We are looking into the possibility of removing the cover over the CCD chip to help remove more fringes. However, this will need to be done in a clean room, as the dust in the lab is significant. Also, continued improvements in laser technology may provide a far superior laser that could be used as the probe laser. The system currently works with optics up to 15.24 cm on a side. The system will be modified to work with full-sized (40 cm) optics.

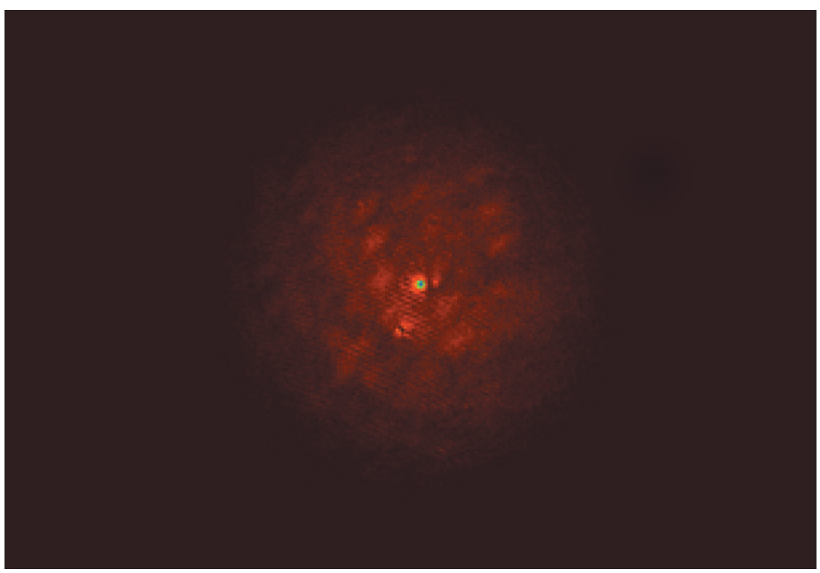

Photothermal image of defect on coated BK7 glass. Field of view is approximately 3 mm X 2 mm.

Time Reversal in a Layered Medium

D. H. Chambers, B. L. Guidry, A. Meyer

We are using a time-reversal array to detect voids between two layers of materials. We have determined the sensitivity of the spectrum of eigenvalues and eigenvectors to the presence of a 4.75-mm-diameter hemispherical bump on the underside of an aluminum slab.

The array is positioned on the surface of a layered material so that acoustic pulses propagate in a direction roughly normal to the layers. These pulses are reflected from both the layer interface and small voids in the interface. The reflected pulses are time-reversed and sent back into the material. This process is iterated until it converges into an eigenstate of the time-reversal operator associated with either a void or the interface.

The eigenstates associated with the interface can be understood in terms of interactions between the array and its image in the interface. We look at the problem of detecting eigenstates associated with voids in the presence of the interface eigenstates.

The figure shows the spectrum of eigenvalues for an aluminum slab with and without a 4.75-mm-diameter hemispherical bump on the underside. There is a slight increase in the magnitude of the first three eigenvalues and a larger decrease in eigenvalues 6, 7, and 8.

A simplified analytical model predicts the increase of low order eigenvalues, but does not do as well for eigenvalues 6, 7, and 8. Though not shown here, the eigenvectors are more sensitive to the presence of the bump than the spectrum of eigenvalues, for both modeling and experiment.

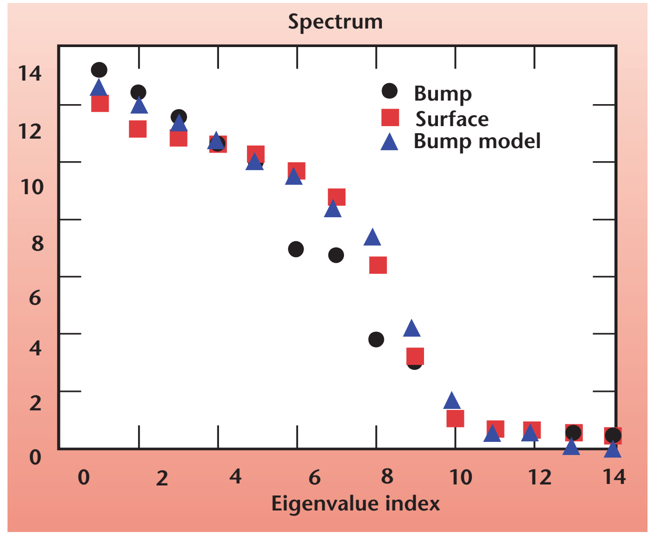

Spectrum of eigenvalues for an aluminum slab with and without a 4.75-mm-diameter hemispherical bump on the underside.

Implementation of a Cone-Beam Reconstruction Algorithm

Y.-M. Wang, P. Roberson

The objective of this project was to evaluate and implement an efficient cone-beam reconstruction algorithm that is capable of reconstructing the full detector view of an object, without distortion of image due to the cone-beam effects.

A CCAT system for a large variety of objects has been developed at the Center for Nondestructive Characterization. CCAT is a micro-focus x-ray source coupled to an amorphous silicon flat-panel detector, used to acquire digital radiography (DR) and CT data. The CCAT system has a large detector area and a small source-to-detector distance, creating an extremely high cone angle from the x-ray source.

CCAT will require the implementation of a cone-beam reconstruction algorithm if we want to take advantage of the full detector area without distortion caused by the large cone angle. The CCAT system will require an exact 3-D reconstruction algorithm capable of reconstructing a large cone angle of 15° to 20°. Exact cone-beam algorithms are relatively new and are only recently maturing to the point where they are becoming a viable solution.

There are a number of these algorithms in existence today, including one that is being developed at LLNL, called LCONE_CCG. The practical obstacle for applying an exact reconstruction algorithm in the CCAT system is the computational complexity of the algorithm, which is on the order of N^5 in most of the cases.

During the past year, an intensive review has been conducted on a variety of reconstruction algorithms for the cone-beam configurations. The emphasis has been concentrated on the practical approximation algorithms that can be implemented in our CCAT system.

With the consideration of the computational complexity and implementation of the potential algorithms, we finally came to a conclusion that the best choice is an algorithm that is incorporated with the use of the Feldkamp algorithm and has scan geometry compatible with our CCAT system.

One reason for the use of the Feldkamp algorithm as an intermediate stage is that we have invested a considerable resource in the implementation of the algorithm to our Linux cluster. We have also made the parallel version available in both the local Linux cluster and LLNL's supercomputers (see report by H. Jones, *et al.,* in this document).

Finally, one algorithm that satisfies our requirement is Lin's algorithm. The reconstruction scheme can be summarized as follows:

1) apply Feldkamp to the circular scan data, obtaining an image in Fourier space;
2) apply Feldkamp to the linear scan data, obtaining an image in Fourier Space;
3) patch in the missing parts of data in the Feldkamp reconstruction of the circular scan with the relevant pieces from the Feldkamp reconstruction of the linear scan in Fourier space;
4) use the inverse Fourier transform to obtain the final image in the image space.

As we can see from the above procedure, the center part of the algorithm is the data patch in Fourier space. We might have difficulties in the implementation of the algorithm; however, we concluded that the risk could be mitigated with a careful selection of smoothing technique in the data patch process.

Meanwhile, examples given in a reference paper demonstrated that the algorithm gives reasonable reconstruction for an 18° cone-beam scanner. Therefore, we are confident that we should be able to implement it for our CCAT system with a reasonable effort.

We have finished the identification of the algorithm for our CCAT system. The feasibility has been confirmed with our current Feldkamp capability. The implementation of a cone-beam reconstruction algorithm for CCAT will provide the opportunity to use the CCAT system to its full potential. This will open up a wealth of new opportunities for programmatic work for NDE. Meanwhile, our current cone-beam reconstruction algorithm (Feldkamp) can only reconstruct approximately 20% of the detector area on CCAT without considerable distortion. It is imperative for us to obtain a full cone-beam reconstruction capability in NDE. We think that we should proceed to the implementation of the algorithm in the next fiscal year.

Quantitative NDE for Ceramic Processing Defects

D. Chinn, C. Logan

Our objective is to understand the response of a suite of NDE methods to known flaws in ceramics. The overall approach is to apply NDE methods to intentionally-flawed ceramic specimens of Al_2O_3 and BeO. Dimensional inspection, density measurements, swipe analysis (for BeO), film radiography, and candling are complete. Ultrasonic characterization is underway.

We selected Brush Wellman to make the specimens for our analysis, and approached them with a list of potential defect types compiled from past experience and internal consultations. They manufactured four defect types—inclusion, unsintered agglomerate, microcracks-thermal, and delamination—in two ceramics, Al_2O_3 and BeO. They also made blanks for recreating (at LLNL) a type of machining damage observed several years ago.

We have 24 specimens (15 flawed) made of each material. Specimen geometry is shown in Fig. 1. This geometry provides orientation cues for most cross-sectional views and offers two sets of parallel surfaces for ultrasonic velocity measurements. All as-received specimens were below the DOE release limits for BeO surface contamination. While measurable contamination was observed on about half the specimens, there was no statistically significant difference between BeO and Al_2O_3 specimens.

We explored a potential alternative to water immersion for ultrasound—a pulsed Nd:YAG laser was used to generate ultrasound, detected on the opposite side by an air-coupled transducer. Figure 2 shows a typical waveform from the air-coupled receiver.

We found these specimens too thick and the ceramic too intensely scattering for our usual candling method to work. The machining damage blanks are thinner, 7 mm, and light does pass through. These specimens contain no defects at present. We measured light transmission as a function of wavelength in a standard spectrophotometer for one specimen of each ceramic type.

Al_2O_3 transmission is insufficient to measure, but we observed structure in the light transmission of BeO.

Film radiography is complete for all specimens. It appears that in every case where we intended to have a defect, it can be discerned on one or the other of two radiographic views. Figure 3 shows an unsintered agglomerate in one Al_2O_3 specimen.

One unexpected result is evident in radiographs of specimens with inclusions. It appears that Mo inclusions strongly affected the sintering process in the BeO. Much work remains to completely characterize this, but the radiographs reveal a large volume of low x-ray opacity centered on the Mo inclusions.

We are exploring the feasibility of microwave imaging, with the University of Missouri-Rolla. X-ray CT, dye penetrant, optical coherence tomography, IR, and ultrasound will be completed at LLNL in FY03.

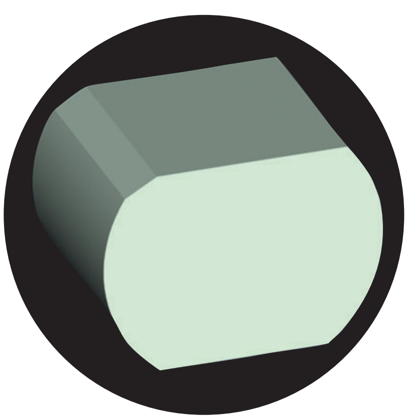

Figure 1. *Ceramic specimen geometry. Distance between each pair of parallel surfaces is 22 mm.*

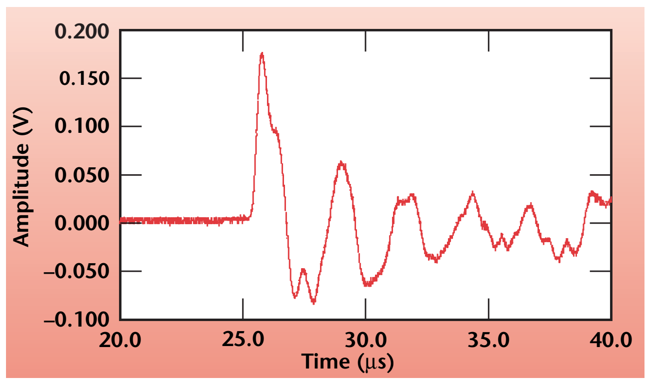

Figure 2. *Ultrasonic waveform detected in non-contacting transmission through a ceramic specimen.*

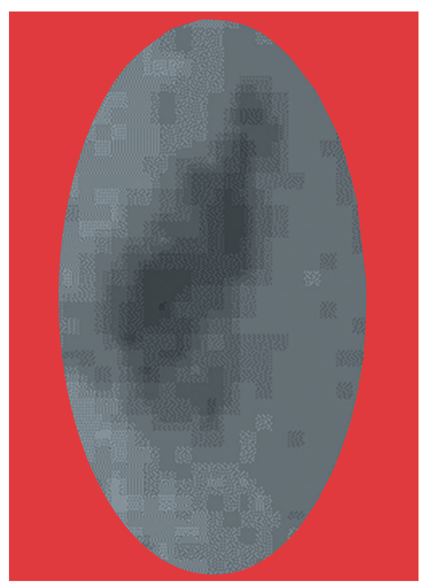

Figure 3. *Portion of a film radiograph revealing an unsintered agglomerate.*

Developments in Sonic IR NDE

W. O. Miller

Sonic IR shows promise as a new NDE technique that can detect flaws, such as tightly closed cracks, that are difficult to detect with other methods. This project is extending the reliability and reach of this technology, and also providing this capability at LLNL.

IR NDE methods have several unique advantages, including noninvasive and non-contact inspection, portability, simplicity and relatively low cost. IR NDE is well-suited for evaluating certain material characteristics and flaw types, including temperature, thermal properties, closed cracks, and buried pockets.

Sonic IR works by dynamically exciting the part being tested with an acoustic probe that is in physical contact with the part. Any resulting differential motion across a crack face creates heat by friction, and a traditional IR camera images the transient temperature rise at the crack (Fig. 1). The camera can image a large area, so scanning is not required. We have found that the method is generally applicable to a wide variety of materials and flaw types.

Our FY02 efforts have focused on enhancing and improving this technology, with emphasis on hardware integration, image processing, computer modeling, and basic analysis of the process physics.

We have constructed a Sonic IR test facility centered around a state-of-the-art IR camera with a high frame rate to capture short transients, and an industrial 30-kHz welder as the acoustic source.

The following accomplishments are also noteworthy.

Flaw quantification

This signal processing method is able to extract and quantify flaw features such as crack length and depth. It relies on comparing the IR data to exact analytical results for prototypical flaws, using the flaw geometry as fitting parameters. A preliminary software version has been encoded which successfully extracts crack geometry.

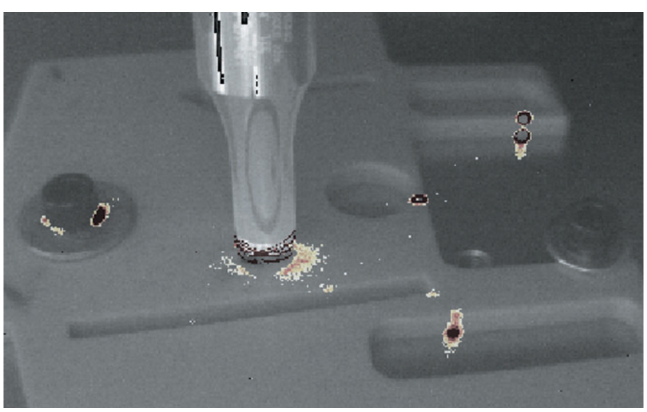

Figure 1. *Sonic IR image showing damage locations (black/orange/white areas) on a machined aluminum oxide plate. The acoustic probe is in the image center.*

Image synthesis

This signal processing method fits the raw image data into a mathematically precise series expression, creating a synthesized image. The series expression allows exact mathematical manipulation for image enhancement, which increases the detection range of the method (*e.g.*, deeper flaws can be detected). We now have a preliminary software version which exemplifies all these features (Fig. 2).

Inspection limits

The current effort on this task is to analytically and numerically predict the frictional heating of a generic crack subject to a cyclic acoustic load. When this is coupled with a conduction model for heat diffusion, then the inspection limits can be found. The analytical effort is nearly complete.

Damage limits

Experience has shown that Sonic IR can damage brittle parts with existing flaws. This effort attempts to define the damage threshold by considering established theory for fatigue crack propagation using the Paris equation. The results indicate that only relatively large existing cracks are at risk.

Future directions

The goal for FY03 is a deployable capability. Further enhancements to the method will be evaluated, including a virtual model of the process physics, and a study of optional acoustic sources. Finally, extensive applications of the method will be made to construct a valuable experience base.

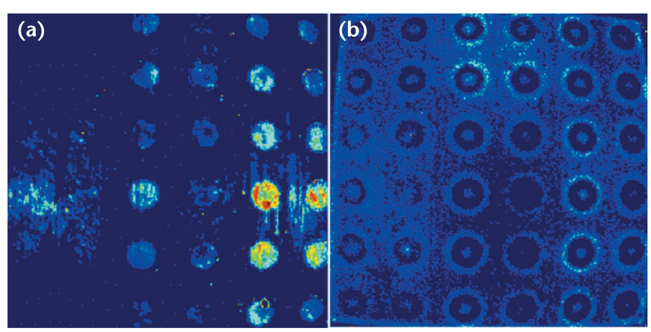

Figure 2. *Example of image synthesis: (a) raw IR image of plate with holes at various depths; (b) synthesized image with time-derivative processing.*

Evaluating CMOS-Based X-Ray Detectors

D. Schneberk, D. Rikard, H. E. Martz, Jr.

The introduction of Complementary Metal-Oxide Semiconductor (CMOS)-based x-ray detectors has generated considerable interest as a low-cost high-performance alternative to amorphous-silicon (Am-Si) or amorphous-selenium (Am-Se) panels. We have evaluated three different types of CMOS imagers.

For Am-Si or Am-Se panels, available pixel sizes are 127 to 400 µm and 139 µm, respectively. CMOS panels support pixel sizes down to 50 µm. In addition, CMOS panels benefit from the large manufacturing expertise in configuring silicon-based devices.

While the current arrays are 2 and 4 in. square, we think CMOS x-ray detectors in 8-in.-square to 12-in.-square formats with the same small pixel size are on the horizon. At least three different projects at LLNL could benefit from large-format small-pixel-size detectors: high-magnification micro-focus DR and CT of HE detonators; DR/CT imaging of high explosives, simulants, and false alarm items; and DR/CT of weapons components.

We evaluated three different types of CMOS imagers: a RAD-ICON 1-k-×-1-k CMOS panel with a LANEX FINE scintillator; a similar RAD-ICON 1-k-×-1-k panel with a 20-ml lead screen; and, a HAMAMATSU 2.2-k-×-2.2-k (4.5-in.-×-4.5-in.) panel that includes columnar CsI as the scintillator bonded to the CMOS array. A similar set of radiographic objects was imaged on the three different detectors to evaluate the sensitivity, linearity, persistence, and image fidelity. All three of the detectors included spatial resolution down to 8 lp/mm, as measured with a line-pair gauge. The RAD-ICON panel with the LANEX FINE had the best spatial resolution of the three, showing the most modulation at 8 lp/mm. However, the RAD-ICON panels showed the most persistence (latent image from a previous exposure). Some of the objects were radiographically opaque at low energy, and for the RAD-ICON panels this pattern became part of the background image for every subsequent image.

This effect was less for the HAMAMATSU panel. To illustrate some of the promise of larger format CMOS arrays we imaged a 20-lp/mm line-pair gauge with a micro-focal source, magnifying the small section of the gauge onto the HAMAMATSU panel. Figure 1 contains an image of this configuration.

In addition to standards objects, we radiographed HE simulants, HE false-alarm items and HE detonators. Using resources from other projects, we are presently configuring the HAMAMATSU panel for use in the KCAT micro-focal cabinet as the detector for this CT system.

The CMOS panel with the lead screen provided a different means for imaging at high energy. The mechanism with the lead screen is different: with this detector we are measuring the electron output from the lead screen, not the photon output from a scintillator. Tests conducted here have shown this detector to have every bit of the spatial resolution as with the scintillators, but an intrinsic resistance to low energy x rays.

We routinely perform DR and CT with a 9-MV Linac for scanning dense objects and assemblies. One difficulty in this imaging is the preponderance of low-energy scatter. Both the LANEX-FINE and CSI scintillators are made for medical sources and are particularly sensitive to low-energy x rays. Most of these lower-energy x rays carry very little information about the object, and are the result of scatter interactions from the fixturing in the beam path.

Figure 2 includes an image of the 1-in. steel step-wedge acquired at 450 kV using the Pb-Screen CMOS detector. Analysis of this image shows the detector preferentially records the higher energy content of the spectrum with no loss in spatial resolution. We are currently exploring the possibility of configuring larger versions of the Pb-Screen panel with both RAD-ICON and HAMAMATSU.

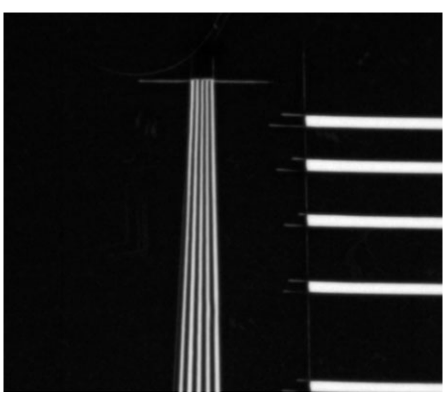

Figure 1. *Image of the end of a 20-lp/mm line-pair gauge.*

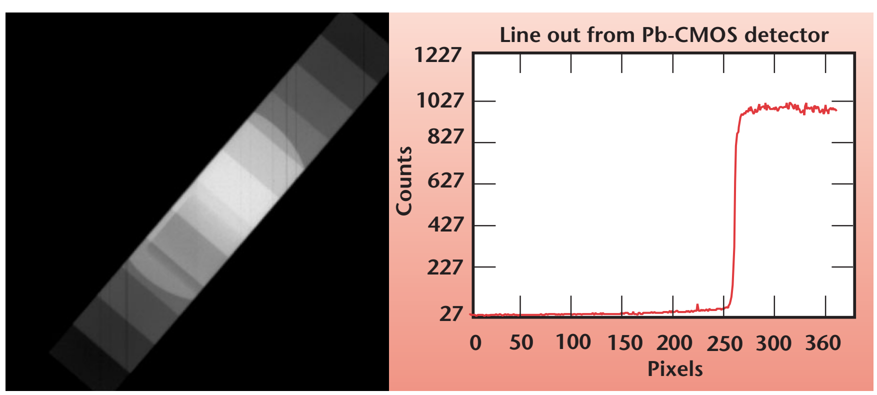

Figure 2. *Image of steel step-wedge and line-out through the wedge from a Lead Screen RAD-ICON CMOS panel.*